Trans-ruthenium(II) complexes for photoactivated cChemotherapy: from design to anticancer activity

Verbeet, W.

Chapter 3

Building a *Trans* Dissymmetric Ruthenium(II) Complex for Sequential Ligand Photosubstitution

Abstract: In pursuit of better understanding the photochemistry of *trans* ruthenium(II) complexes, a series of *trans*-complexes $[Ru(HL)(X)(Y)](PF_6)_2$ has been studied, where X = Y is methyl(2-thioethanol) (MTE; [**1a**]$(PF_6)_2$), acetonitrile (ACN; [**2a**]$(PF_6)_2$), or pyridine (Py; [**3a**]$(PF_6)_2$) based on the planar tetrapyridyl ligand HL (di([2,'2-bipyridin]-6-yl)amine) as well as its *N*-methyl analogue MeL $[Ru(MeL)(X)(Y)](PF_6)_2$ ([**1b**]$(PF_6)_2$–[**3b**]$(PF_6)_2$). While the compounds are thermally stable in the dark, in all complexes irradiation with blue or green light induced photosubstitution of the axial ligands. Red light photosubstitution of both ligands was only observed for $[\mathbf{3a}]^{2+}$ and $[\mathbf{3b}]^{2+}$. Using this knowledge it was possible to photochemically prepare the dissymmetric complex $[Ru(MeL)(Py)(MTE)](PF_6)_2$ ([**4b**]$(PF_6)_2$). Strikingly, sequential release was observed for this complex of Py with red light, followed by MTE with green light, providing the first example of selective, wavelength-dependent photosubstitution in a dissymmetric *trans*-ruthenium(II) complex. The kinetics of all photosubstitution reactions was determined, thus providing the first quantitative analysis of *trans* effects in excited, triplet states of ruthenium complexes.

This work from W. Verbeet, A. Jiao, M.A. Siegler, S. Bonnet, will be submitted for publication. *Manuscript in preparation.*

3.1 Introduction

Light allows for exquisite control over the ligand exchange reactivity in ruthenium(II)-based complexes. This principle has been used for diverse applications, ranging from photocatalysis to photomedicine. The tunable triplet excited states of polypyridyl ruthenium complexes can indeed be steered towards a variety of light-induced photophysical and photochemical processes, such as phosphorescence, energy transfer, electron transfer, ligand isomerization, or ligand photosubstitution.[1–3] The latter has been employed to trigger the photorelease of cytotoxic inhibitors in an anticancer treatment modality called photo-activated chemotherapy (PACT).[4] Typically, polypyridine ligands in ruthenium-based PACT compounds are often combinations of tridentate 2,2':6',2'-terpyridine (tpy) and/or bidentate 2,2'-bipyridine (bpy) ligands. In the $[Ru(tpy)(bpy)(L)]^{2+}$ photocage for example, the monodentate position in the first coordination sphere allows for the incorporation of photolabile ligands such as pyridine,[5] pyrimidine,[6] nitrile,[7] amine,[8] or thioether.[9] Other ruthenium-based photocages have been extensively studied, such as those based on the *cis*-$[Ru(bpy)_2(L_2)]^{2+}$ architecture, where L is a N- or S-based bidentate chelate.[10–13] The photochemistry of the analogous complexes *cis*-$[Ru(bpy)_2(L')(L'')]^{2+}$, where L' and L'' are N- or P-based monodentate ligands such as pyridines, nitriles, imidazoles or phosphines, has been thoroughly studied both experimentally and theoretically. Typically, the first photosubstitution is efficient but the second is much slower (e.g., when L' = L'' = pyridine) or does not take place at all (e.g., when L' = amine and L'' = phosphine).[14–18]

Much less information is available on the photoreactivity of *trans* ruthenium(II) complexes. *Cis* complexes are usually more stable thermally, while *trans*- and *cis*-$[Ru(bpy)_2(X)(Y)]^{2+}$ complexes do show cis-to-trans isomerization upon light irradiation, leading to complex mixtures and difficult kinetic analysis. *Trans* ruthenium complexes are, however, of particular relevance due to the central role of a classical concept in coordination chemistry called the *trans* effect. Due to the centrosymmetric nature of the d orbitals, monodentate ligands situated in *trans* position in the coordination sphere of a metal complex, share the *trans* lobes of the same d orbital(s). As a consequence, the bond distance and the kinetics of ligand substitution of any given ligand in the coordination sphere of the metal ion are usually strongly influenced by the ligand in *trans* position. These two concepts are called the *trans* influence and *trans* effect, respectively. Basically, ligands with a strong *trans* effect facilitate substitution of the ligand *trans* to them. Coordination chemists have tabulated the *trans* effect of classical monodentate ligands and established a *trans* effect series, from ethylene, CN^-, or CO on the side of the ligands that labilise their *trans* ligands particularly well, to OH^-, OH_2, and F^- that are very bad at it.[19]

The *trans* effect has been well described for ground-state metal complexes, and has important applications such as the industrial production of the approved anticancer drug cisplatin, without traces of its inactive isomer.[20] Several teams have focused their efforts on understanding the specific biochemical properties of *trans* complexes, in particular for cancer treatment.[21,22] However, little is known on what the *trans* effect series becomes when a metal complex is excited with light. In other words, what is the influence of *trans* effects on the photoreactivity of photolabile ruthenium complexes, and what is the effect of excitation of a ruthenium complex on the *trans* effect of a given monodentate ligand?
This question can be illustrated by two examples reported by the Etchenique group. In a series of *cis*-$[Ru(bpy)_2(L)(ACN)]^{2+}$ complexes, where L is NH_3, PPh_3 (triphenylphosphine), PMe_3 (trimethylphosphine) or ACN, variation of L primarily affected the Ru–N(bpy) bond distance *trans* to L, indicating a *trans* influence.[23] However, both the Ru–N(ACN) bond length and ACN photosubstitution quantum yield were largely independent of L, demonstrating the expected absence of a *trans* effect or *trans* influence in the *cis*-complex. In another study, photosubstitution of imidazole (ImH) was shown to occur more efficiently from *trans*-$[Ru(bpy)_2(PMe_3)(ImH)]^{2+}$ than from its *cis* isomer under green light irradiation with quantum yields of 0.23 and 0.10, respectively. The latter example illustrates the stronger *trans* effect of phosphines compared to that of pyridines.[24] However, thorough understanding of *trans* effects in photosubstitution reactions is currently lacking due the limited data available on the photosubstitution of ruthenium(II) complexes with *trans* geometries.

To fill this knowledge gap, we focused here on the rigid tetrapyridyl ligands di([2,'2-bipyridin]-6-yl)amine (HL), and its *N*-methylated analogue (MeL). When coordinated to a metal center in octahedral geometry, these ligands leave only two *trans* positions in the coordination sphere (Figure 3.1). Although photosubstitution of methyl(2-thioethanol) (MTE) from tetrapyridyl complexes *trans*-$[Ru(H_2bapbpy)(MTE)_2]^{2+}$ (H_2bapbpy = 6,6'-bis(2-aminopyridyl)-2,2'-bipyridine) and *trans*-$[Ru(H_2biqbpy)(MTE)_2]^{2+}$ (H_2biqbpy = 6,6'-bis(2-aminoisoquinolyl)-2,2'-bipyridine) have been reported, only a single MTE ligand was released upon blue light irradiation (Figure 3.1a).[25] To investigate the possibility to photorelease two monodentate ligands upon irradiation with longer wavelengths, we prepared a series of new symmetric bis-thioether complexes $[Ru(HL)(L')(L'')](PF_6)_2$ where L' = L'' = MTE ([**1a**]$(PF_6)_2$), and their acetonitrile (ACN; [**2a**]$(PF_6)_2$) and pyridine (Py; [**3a**]$(PF_6)_2$) analogues. The *N*-methyl derivatives $[Ru(MeL)(L')(L'')](PF_6)_2$ ([**1b**]$(PF_6)_2$ – [**3b**]$(PF_6)_2$) were prepared as well to investigate the influence of the electron density of the tetrapyridyl ligand on the photosubstitution reactivity. All complexes were found to be photolabile using visible light irradiation; the kinetics of all photosubstitution reactions were quantified under blue, green, or red light, to investigate the effect of *trans* ligands were on the photoreactivity of the complex at different wavelengths. Only the bis-pyridine complexes appeared to be photolabile in red light, which allowed us to prepare photochemically the

dissymmetric complex [Ru(MeL)(L')(L")]$(PF_6)_2$ ([**4b**]$(PF_6)_2$) containing two different axial ligands, i.e., L' = MTE and L" = Py. The photolability of the thioether vs. pyridine ligand of this dissymmetric complex was also quantified upon irradiation with blue, green or red light. Based in the analysis of the *trans* effects of the ligands MTE, Py, ACN, and OH_2 in the excited state of all metal complexes [**1b**]$^{2+}$ – [**4b**]$^{2+}$, we were able to realize the sequential photosubstitution of Py first, followed by MTE, using consecutive irradiation with red and green light, respectively, thus showing exquisite control over the photoreactivity of the complex.

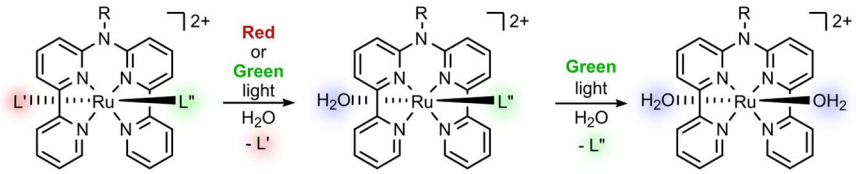

[**1a**]$(PF_6)_2$, R = H, L' = L" = MTE
[**1b**]$(PF_6)_2$, R = CH_3, L' = L" = MTE
[**2a**]$(PF_6)_2$, R = H, L' = L" = ACN
[**2b**]$(PF_6)_2$, R = CH_3, L' = L" = ACN
[**3a**]$(PF_6)_2$, R = H, L' = L" = Py
[**3b**]$(PF_6)_2$, R = CH_3, L' = L" = Py
[**4b**]$(PF_6)_2$, R = CH_3, L' = Py, L" = MTE

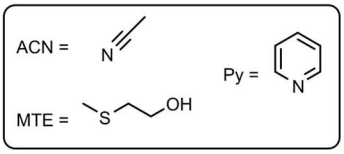

Figure 3.1 Schematic overview of sequential photosubstitution of axial ligands X and Y from *trans*-tetrapyridyl ruthenium(II) complexes presented in this study.

3.2 Results

3.2.1 Synthesis

Ligand HL was synthesized via a modified Buchwald-Hartwig coupling between (2,2'-bipyridine)-6-amine (NH_2-bpy) and (2,2'-bipyridine)-6-bromide (Br-bpy) using 1,3-bis(diphenylphosphino)propane (dppp) instead of 2,2'-bis(diphenylphosphino)-1,1'-binaphthyl (BINAP) as previously reported (Scheme 3.1).[26] Subsequently, the amine-bridge in HL was methylated with methyl iodide in presence of an excess of potassium hydroxide in DMSO, providing the MeL ligand in good yield. Complexes [**1a**]$(PF_6)_2$ and [**1b**]$(PF_6)_2$ were synthesized in good to excellent yield by reacting the tetrapyridyl ligands HL or MeL, respectively, with [Ru(DMSO)$_4$Cl$_2$] dissolved in MTE.

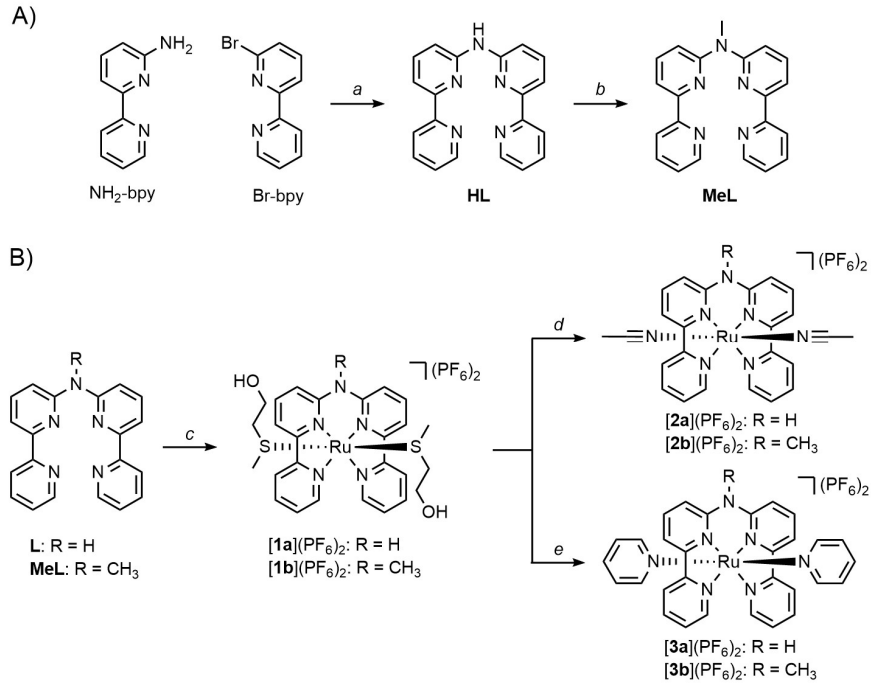

Scheme 3.1 Overview of synthetic routes. A) Synthesis of ligand HL and MeL; *a*) $Pd(dba)_3$, dppp, NaO*t*Bu in toluene, 80 °C, 18 h, 85%; *b*) MeI, KOH in DMSO, RT, 3 hr, 95%. B) Synthesis of complexes [**1a,b**]$(PF_6)_2$ – [**3a,b**]$(PF_6)_2$; *c*) i) $Ru(DMSO)_4Cl_2$ in 2-(methylthio)ethanol, N_2, 150 °C, 3 days for [**1a**]$(PF_6)_2$, 2 days for [**1b**]$(PF_6)_2$; ii) KPF_6 (aq.), 71% for [**1a**]$(PF_6)_2$, 90% for [**1b**]$(PF_6)_2$; *d*) i) ACN, reflux, 5 days for [**2a**]$(PF_6)_2$, 2 days for [**2b**]$(PF_6)_2$; ii) KPF_6 (aq.), 79% for [**2a**]$(PF_6)_2$, 46% for [**2b**]$(PF_6)_2$; *e*) i) Pyridine, N_2, 115 °C, 1 day for [**3a**]$(PF_6)_2$, 2 day for [**3b**]$(PF_6)_2$; ii) KPF_6 (aq.), 93% for [**3a**]$(PF_6)_2$, 77% for [**3b**]$(PF_6)_2$.

From the thioether complexes, the corresponding acetonitrile ([**2a,b**]$(PF_6)_2$) and pyridine ([**3a,b**]$(PF_6)_2$) analogues were synthesized by refluxing [**1a,b**]$(PF_6)_2$ in the desired monodentate ligand as solvent. While all other complexes were pure after washing the precipitate, [**2b**]$(PF_6)_2$ had to be purified by silica gel chromatography. Characterization of all new compounds was performed using NMR spectroscopy, mass spectrometry, elemental analysis, and UV-Vis absorption spectroscopy (see Experimental part and Appendix III).

Since [**4b**]$(PF_6)_2$ contains both MTE and pyridine as axial ligands *trans* to each other, the synthesis could theoretically be performed either by reacting the bis-MTE complex [**1b**]$(PF_6)_2$ with free pyridine, or by reacting the bis-pyridine complex [**3b**]$(PF_6)_2$ with free MTE. However, initial attempts to perform these reactions under thermal conditions resulted in a mixture of the three possible complexes with [**1b**]$(PF_6)_2$ and [**3b**]$(PF_6)_2$ as major thermodynamic products. The reactions were also performed at room temperature by irradiation with 650 nm light (Scheme 3.2), as photosubstitution of thioether or pyridyl ligands from ruthenium (II) polypyridyl complexes has been reported extensively.[27–29] In

such conditions, [**4b**](PF$_6$)$_2$ could not be generated by light irradiation of [**1b**](PF$_6$)$_2$ in an acetone solution containing an excess (> 5 equivalents) of free pyridine because it was essentially photochemically unreactive at such high wavelengths. However, the photoreaction starting from [**3b**](PF$_6$)$_2$ in presence of 10 equivalents of free MTE, provided [**4b**](PF$_6$)$_2$ with a good yield (63%) after isolation by column chromatography. Characterization using NMR spectroscopy, mass spectrometry and elemental analysis confirmed the successful preparation of the dissymmetric complex [**4b**](PF$_6$)$_2$.

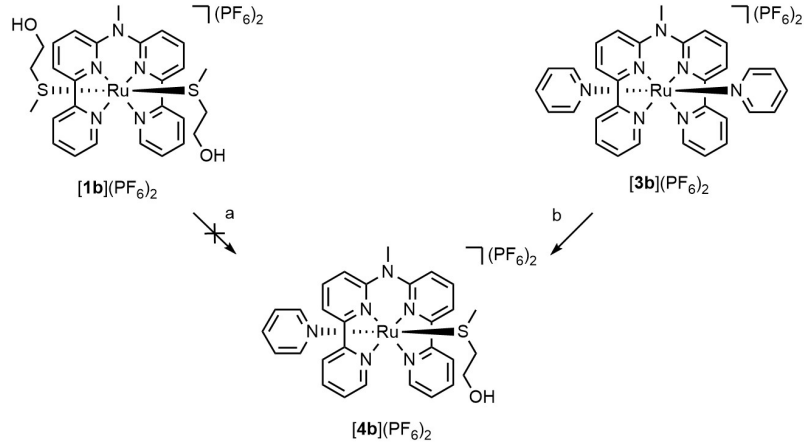

Scheme 3.2 Schematic overview towards the synthesis of [**4b**](PF$_6$)$_2$ via red light (650 nm) irradiation. *a*) Pyridine in acetone, N_2, 25 °C, 1 h; *b*) 2-(methylthio)ethanol in acetone, N_2, 25 °C, 1 h, 63%.

3.2.2 Crystal structures

Single crystals of [**1a**](PF$_6$)$_2$, [**1b**](PF$_6$)$_2$•TPPO (TPPO = triphenylphosphine oxide), [**2b**](PF$_6$)$_2$, [**3b**](PF$_6$)$_2$ and [**4b**](PF$_6$)$_2$ suitable for X-ray diffraction were obtained via vapor diffusion of diethyl ether into a solution of the complex in acetone, or a THF/acetone mixture (Figure 3.2 and Table 3.1). For [**1b**](PF$_6$)$_2$, TPPO was added to the complex solution in acetone, and ended up as solvate in the crystal structure. While [**1b**]$^{2+}$ is an analogue of [**1a**]$^{2+}$, differences between the crystal structures of the two complexes were observed. Firstly, a larger difference between the Ru-N1 and the Ru-N2 distances was found in [**1a**]$^{2+}$, compared to [**1b**]$^{2+}$ (Ru-N1 – Ru-N2 = ~0.20 Å and ~0.07 Å, respectively), showing the more open geometry of the NH-bridged analogue. Also, a difference of ~0.1 Å in Ru-S distances was observed in [**1a**]$^{2+}$, while both Ru-S distances are near identical in [**1b**]$^{2+}$. Furthermore, a larger N1'-Ru-N2 bond angle was observed for [**1a**]$^{2+}$ than in [**1b**]$^{2+}$ (176° and 172°, respectively), with a torsion angle of the coordinated pyridyl N-atoms (N1-N2-N2'-N1') larger for [**1a**]$^{2+}$ than for [**1b**]$^{2+}$ (-5.6° and 2.4°, respectively). In other words, the methyl group in **MeL** ligand prevents the helical "twisting" of the tetrapyridyl ligand upon coordination to ruthenium. However, [**1a**]$^{2+}$ and [**1b**]$^{2+}$ are far more planar compared to the previously reported [Ru(H$_2$bapbpy)(MTE)$_2$]$^{2+}$ and [Ru(H$_2$bapbpy)(MTE)$_2$]$^{2+}$ in which the tetrapyridyl ligand to a helical conformation around the metal center.[25] The τ_4 value, a

structural distortion parameter indicative for a square-planar geometry when τ_4 = 0, is lower for [**1a**]$^{2+}$ (0.05) than for [**1b**]$^{2+}$ (0.11). However, for both [**1a**]$^{2+}$ and [**1b**]$^{2+}$ a similar distortion of the octahedral geometry was observed, with values for the octahedral distortion parameter (Σ) of 68°and 67°, respectively. These results indicate that the subtle modification of **HL** by methylation of the bridging N-atom affects the binding of the tetrapyridyl ligand.

Between the symmetrical methylated complexes [**1b**]$^{2+}$, [**2b**]$^{2+}$ and [**3b**]$^{2+}$, small differences in the bond lengths between the polypyridyl ligand and ruthenium center were observed. The Ru-N bond lengths for the MeL pyridyl N-atoms are comparable, with Ru-N1 = ~2.096 Å and Ru-N2 = ~2.020 Å. However, variations in the metal–axial ligand bond lengths were observed among the complexes. The Ru–S bonds in [**1b**]$^{2+}$ measured approximately 2.370 Å, reflecting the larger van der Waals radius of sulfur atoms. In contrast, shorter Ru–N distances were found in [**2b**]$^{2+}$ (~2.026 Å) compared to the slightly longer Ru-N distances found in the bis-pyridine compound [**3b**]$^{2+}$ (~2.106 Å).These results are similar to those reported earlier for polypyridyl complexes bearing thioether, acetonitrile and pyridine ligands.[30–32] Interestingly, similar bond lengths were observed for the dissymmetric complex [**4b**]$^{2+}$, with Ru-S1 = ~2.363 Å and Ru-N4 = ~2.110 Å, suggesting no significant *trans*-influence in the ground state of the dissymmetric complex. The axial ligands also do not affect the square planar geometry of the MeL ligand, with τ_4 values around 0.11 for all four molecules. A slightly lower octahedral distortion was observed for [**3b**]$^{2+}$ (Σ = 56°) than for [**1b**]$^{2+}$, [**2b**]$^{2+}$ and [**4b**]$^{2+}$ (Σ = 67°, 61° and 66°, respectively), which we attribute mostly to packing effects. The torsion angle between coordinating pyridyl nitrogen atoms in **HL** (N1-N2-N2'-N1') was twice larger in [**1a**]$^{2+}$ (-5.6°) than in the MeL analogue [**1b**]$^{2+}$ (2.1°). While no torsion was observed for acetonitrile complex [**2b**]$^{2+}$, angles of 3.5° and 1.0° were found for [**3b**]$^{2+}$ and [**4b**]$^{2+}$, respectively. Interestingly, the MeL containing complexes [**1b**]$(PF_6)_2$ – [**4b**]$(PF_6)_2$ all appear to appear to be coordinated in a "saddle-shape" geometry, while the HL containing complex [**1a**]$(PF_6)_2$ has a more helical geometry.

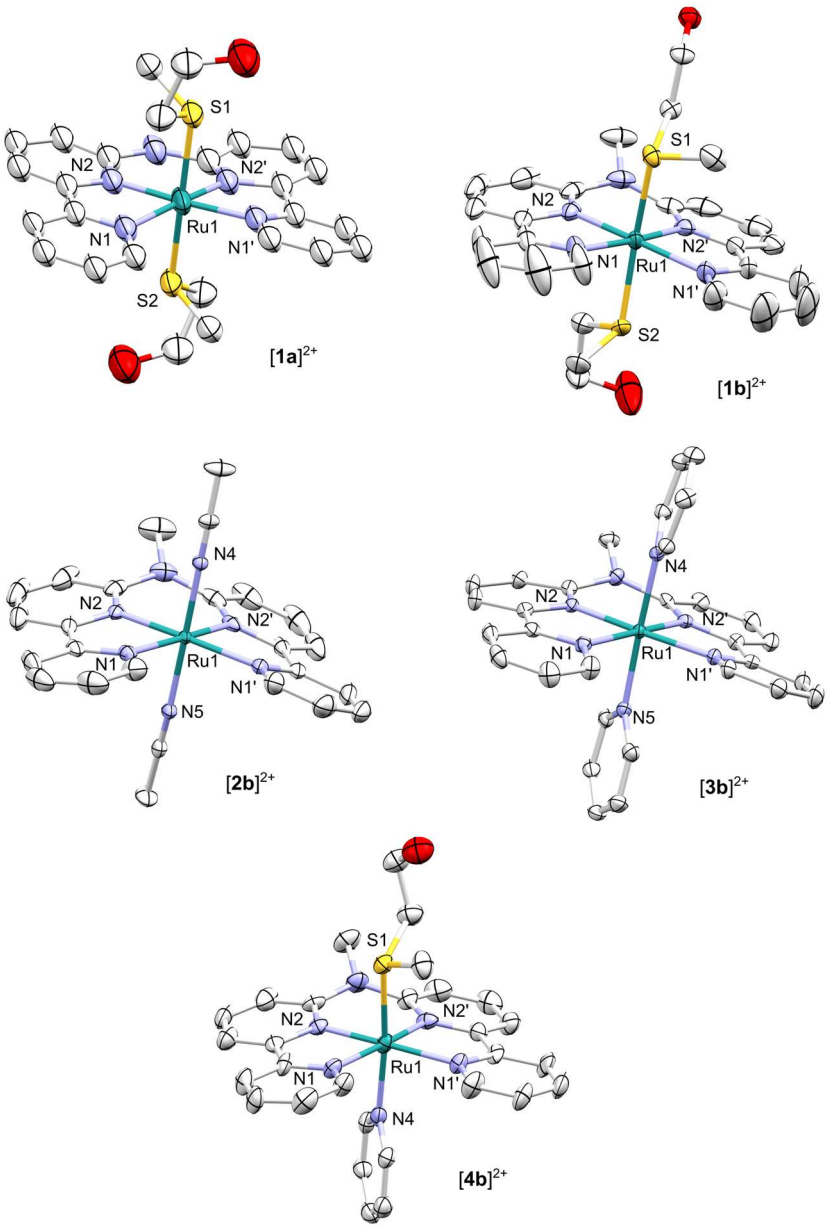

Figure 3.2 Displacement ellipsoid plots (50% probability level) in the crystal structures of complexes [**1a**]$(PF_6)_2$, [**1b**]$(PF_6)_2$(TPPO), [**2b**]$(PF_6)_2$, [**3b**]$(PF_6)_2$ and [**4b**]$(PF_6)_2$. For clarity, hydrogen atoms, counter-ions and lattice solvent molecules have been omitted.

Table 3.1 Selected bond distances (Å) and bond angles (°) for complexes [**1a**]$(PF_6)_2$, [**1b**]$(PF_6)_2$•TPPO, [**2b**]$(PF_6)_2$, [**3b**]$(PF_6)_2$ and [**4b**]$(PF_6)_2$.

	[**1a**]$(PF_6)_2$	[**1b**]$(PF_6)_2$	[**2b**]$(PF_6)_2$	[**3b**]$(PF_6)_2$	[**4b**]$(PF_6)_2$
Ru1-N1	2.141	2.096(3)	2.096	2.095(3)	2.121(7)
Ru1-N2	1.886	2.026(3)	2.020	2.015(3)	2.020(7)
Ru1-N1'	2.174	2.100(2)	2.098	2.095(3)	2.119(7)
Ru1-N2'	1.984	2.023(2)	2.020	2.017(3)	2.028(7)
Ru1-S1	2.432	2.372(1)	-	-	2.363(3)
Ru1-S2	2.324	2.369(7)	-	-	-
Ru1-N4	-	-	2.024	2.109(3)	2.110(9)
Ru1-N5	-	-	2.029	2.104(3)	-
N1-Ru1-N2'	176.7	172.9(1)	171.8	172.0(1)	172.8(3)
N1'-R1-N2	176.4	172.1(1)	171.8	173.7(1)	172.2(3)
S1-Ru1-S2	177.3	173.9(2)		-	-
N4-Ru1-N5	-	-	178.3	178.2(1)	-
N4-Ru1-S4	-	-	-	-	173.9(3)
Torsion angle (◦) N1-N2-N2'-N1'	5.6	2.4(1)	0.0(1)	3.5(2)	1.0(3)
τ_4[a]	0.05	0.11(9)	0.12	0.10(1)	0.11(3)
Σ[b] (°)	68	67(5)	61	56(5)	66(5)

[a] The coordination angles N1-Ru1-N2' (α) and N1'-Ru-N2 (β) were used to calculate τ_4.[33]
$\tau_4 = \frac{360 - (\alpha + \beta)}{141}$

[b] Octahedral distortion parameter Σ was calculated using all *cis* bond angles in the primary coordination sphere.[34] $\Sigma = \sum_{i=1}^{12} |\phi_i - 90|$

3.2.3 Photochemistry

To investigate the thermal stability of the complexes, the UV-Vis absorbance in 1/5 acetone/H_2O solutions of the complexes *vs.* time was monitored over time. Compounds [**1a,b**]$(PF_6)_2$ –[**3a**,**b**]$(PF_6)_2$ and [**4b**]$(PF_6)_2$ were found to be thermally stable for at least 2 h in solution in the dark at 298 K (Appendix III.2.2). The photochemical reactivity of the symmetric complexes was then investigated by monitoring the ^{1}H-NMR spectra of [**1a,b**]$(PF_6)_2$ – [**2a**,**b**]$(PF_6)_2$ in 1/5 acetone-d6/D_2O and [**3a**,**b**]$(PF_6)_2$ in 1/3 acetone-d6/D_2O at 298 K upon irradiation with white or green (530 nm) light. As shown in Figure 3.3 for [**3b**]$^{2+}$ upon green (505 nm) light irradiation for 90 min, the characteristic signals of free pyridine at 8.38, 7.72 and 7.31 ppm appeared. Additionally, the doublet at 9.74 ppm corresponding to a C-H aromatic proton of MeL was initially replaced by a doublet at 9.67 ppm for the

intermediate $[\mathbf{7b}]^{2+}$ (Scheme 3.3), which then converted to a doublet at 9.82 ppm corresponding to the final bis-aqua photoproduct $[\mathbf{8b}]^{2+}$. Similar reactivity was observed for the two other symmetric complexes in these conditions, with signals appearing for free MTE at 3.60 ppm (triplet), free acetonitrile at 1.93 ppm (singlet), and free pyridine at 8.38 ppm (multiplet) upon irradiation of $[\mathbf{1a},\mathbf{b}]^{2+}$, $[\mathbf{2a},\mathbf{b}]^{2+}$, or $[\mathbf{3a},\mathbf{b}]^{2+}$, respectively. These results indicate that $[\mathbf{1a},\mathbf{b}]^{2+}$ – $[\mathbf{3a},\mathbf{b}]^{2+}$ undergo two–step photosubstitution of the axial ligands in presence of water, during which intermediates $[\mathbf{5a},\mathbf{b}]^{2+}$ – $[\mathbf{7a},\mathbf{b}]^{2+}$ are formed first, where one axial ligand is replaced by a H_2O molecule, before photosubstitution of the second non-aqua ligand takes place (Scheme 3.3).

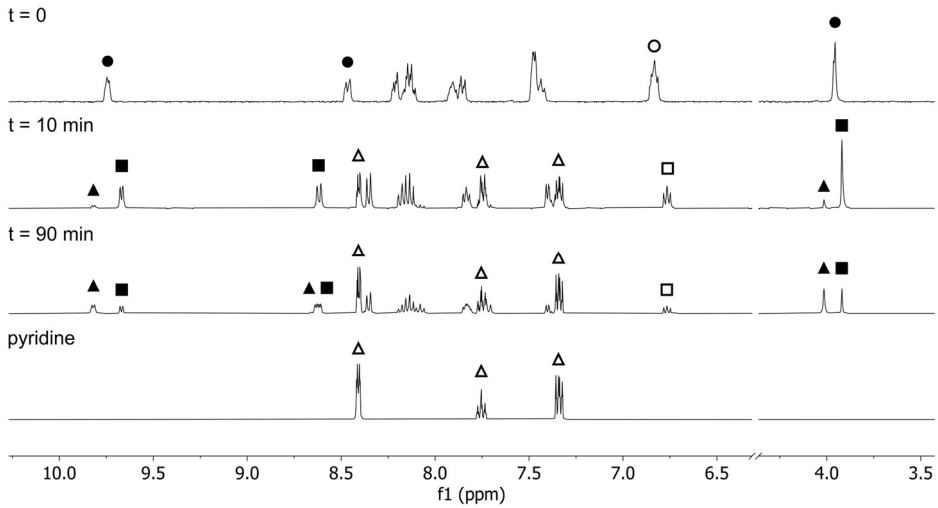

Figure 3.3 Time-evolution of the ^{1}H-NMR spectra evolution of $[\mathbf{3b}](PF_6)_2$ (● for **MeL** protons, ○ for coordinated pyridine) in 1/3 acetone-d6/D_2O at 298 K upon irradiation with green light (530 nm for 90 minutes). Symbols indicate mono-aqua intermediate $[\mathbf{7b}]^{2+}$ (■ for **MeL** protons, □ for coordinated pyridine), bis-aqua photoproduct $[\mathbf{8b}]^{2+}$ (▲), and free pyridine (△).

To be able to quantify the kinetics of Steps 1 and 2 in Scheme 3.3 and to evaluate how changing the nature of the axial ligands and methylating the bridging amine of the tetrapyridyl ligand affects the light absorption properties of the complexes, the UV-Vis absorption spectra of complexes $[\mathbf{1a},\mathbf{b}]^{2+}$ – $[\mathbf{3a},\mathbf{b}]^{2+}$ were first recorded in 1/5 acetone/water. Typical ^{1}MLCT absorption bands culminating between 430 and 485 nm were observed, which are quintessential for polypyridyl ruthenium(II) complexes containing two thioether, nitrile, or pyridine ligands (Table 3.2).

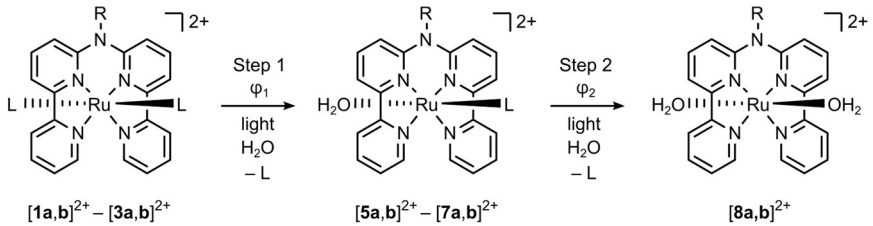

Scheme 3.3 Schematic representation of photosubstitution of axial ligands L in [**1a**,**b**]$^{2+}$ – [**3a**,**b**]$^{2+}$ in presence of H_2O; φ_1 and φ_2 are the photosubstitution quantum yields of Step 1 and Step 2, respectively. [**1a**]$^{2+}$ – [**8a**]$^{2+}$: R = H; [**1b**]$^{2+}$ – [**8b**]$^{2+}$: R = Me; [**1a**,**b**]$^{2+}$, [**5a**,**b**]$^{2+}$: L = MTE; [**2a**,**b**]$^{2+}$, [**6a**,**b**]$^{2+}$: L = acetonitrile; [**3a**,**b**]$^{2+}$, [**7a**,**b**]$^{2+}$: L = pyridine.

A bathochromic shift was observed of the ^{1}MLCT bands of [**3a**,**b**]$^{2+}$ (~486 nm) compared to [**1a**,**b**]$^{2+}$ and [**2a**,**b**]$^{2+}$ (~443 nm and ~432 nm, respectively). Clearly, the pyridine ligands in [**3a**,**b**]$^{2+}$ stabilize the ^{1}MLCT states of the complexes, compared to thioether or nitrile ligands in [**1a**,**b**]$^{2+}$ and [**2a**,**b**]$^{2+}$. For the **MeL** containing analogues [**1b**]$^{2+}$ – [**2b**]$^{2+}$, a slight bathochromic shift of the absorption maximum λ_{max} of the ^{1}MLCT bands was observed, compared to **HL** complexes [**1a**]$^{2+}$ – [**2a**]$^{2+}$. In contrast, identical ^{1}MLCT absorption maxima were found for [**3a**]$^{2+}$ and [**3b**]$^{2+}$. A more obvious difference between the **HL** and **MeL** complexes can be observed when comparing the absorption of red light, with ε at 625 nm being lower for the methylated compounds [**1b**]$^{2+}$ – [**3b**]$^{2+}$ that for the **HL** complexes [**1a**]$^{2+}$ – [**3a**]$^{2+}$.

To evaluate the photoreactivity of the complexes, time evolution of the UV-Vis spectra of solutions of [**1a**,**b**]$^{2+}$ – [**3a**,**b**]$^{2+}$ in a 1/5 acetone/water mixture were recorded upon irradiation with blue (435 nm), green (505 nm) or red light (625 nm). Similar to previous reports and as observed by ^{1}H-NMR, upon irradiation with 435 nm and 505 nm light all complexes showed distinct two-step photoreactions characterized by bathochromic shifts of the ^{1}MLCT band.[29] Strikingly, upon red light irradiation photosubstitution was only observed for the pyridine complexes [**3a**]$^{2+}$ and [**3b**]$^{2+}$. The molar absorption coefficients of these complexes at 625 nm was not significantly higher than those of the other complexes, hence the observed red-light reactivity of the bis-pyridine complexes must be related to differences in excited state properties.

Global fitting of the time-evolution of the absorbance data provided the fitted spectra of the mono-aqua intermediate species [**5a**,**b**]$^{2+}$ – [**7a**,**b**]$^{2+}$ and of the bis-aqua final photoproduct [**8a**,**b**]$^{2+}$ (Appendix III.2.2). These fitted spectra indicated that the degree of bathochromic shifting depends on the ligands that are photosubstituted: while both substitution steps resulted in a shift of the ^{1}MLCT band between 20 and 40 nm for MTE in [**1a**]$^{2+}$ and ACN in [**2a**]$^{2+}$ respectively, substitution of the axial pyridine ligands in [**3a**]$^{2+}$ only resulted in a shift of 10 nm.

Global fitting of the time-evolution UV-Vis absorbance data also provided their kinetic reaction profiles (Table 3.2 and Appendix III.2.2). The kinetic curves of the intermediates [**5a**,**b**]$^{2+}$ – [**7a**,**b**]$^{2+}$ during irradiation of complexes [**1a**,**b**]$^{2+}$ – [**3a**,**b**]$^{2+}$ are shown in Figure 3.4. For blue and green light irradiation these traces can be separated into two domains. In the first domain, a positive slope relates to the formation of mono-aqua intermediate [**5a**,**b**]$^{2+}$ – [**7a**,**b**]$^{2+}$ where one axial ligand of the starting complex has been photosubstituted by water. In the second domain, the slope is negative and relates to the decay rate of [**5a**,**b**]$^{2+}$ – [**7a**,**b**]$^{2+\ +}$ to the final products [**8a**,**b**]$^{2+}$ through photosubstitution of the second axial ligand. When comparing the kinetic curves, key differences between the different complexes were observed (Figure 3.4). Firstly, the acetonitrile complexes behaved in a different manner than the thioether and pyridine compounds. In [**2a**]$^{2+}$ and [**2b**]$^{2+}$, photosubstitution of the second ligand begun before completion of the first photosubstitution step, pointing to the higher photoreactivity of intermediates [**5a**]$^{2+}$ and [**5b**]$^{2+}$, compared to all other mono-aqua intermediates. With the thioether and pyridine complexes, photosubstitution of the first axial ligand took place first and go to completion, before the second ligand started to be photosubstituted. Secondly, the photosubstitution rates were dependent on the irradiation wavelength, breaking Kasha's rule which states that "polyatomic molecular entities react with appreciable yield only from the lowest excited state of a given multiplicity". Unlike at shorter wavelength, under red light irradiation the Py complexes [**3a,b**]$^{2+}$ showed a single photosubstitution step characterized by a slower rate than upon blue or green light irradiation (Figure 3.4 E and F). Although less distinct, differences were also observed between the MTE complexes [**1a**,**b**]$^{2+}$ and Py complexes [**3a**,**b**]$^{2+}$ when comparing blue (435 nm) *vs.* green (505 nm) light irradiation. Upon blue light irradiation, the similar slopes observed for the initial formation of [**5a**,**b**]$^{2+}$ and [**7a**,**b**]$^{2+}$ (green and red lines, respectively, in Figure 3.4 A–D) indicate that the rates of the first photosubstitution steps were neither influenced by the nature of the leaving ligand nor by the N-methylation of the tetrapyridyl ligand. However, the rates of the second step were significantly lower for the **MeL** complexes, while the Py complex [**3b**]$^{2+}$ reacted faster than its MTE analogue [**1b**]$^{2+}$ (Figure 3.2 A and B). In contrast, upon green light irradiation rates of the first step were influenced only by the nature of the leaving ligand, with release of MTE ligands in [**1a**,**b**]$^{2+}$ being slower than release of the Py ligands in [**3a**,**b**]$^{2+}$ (Figure 3.2 C and D), while methylation of the N bridge did not change the rates much. This effect was reversed for the rates of the second step: methylation of the tetrapyridine ligand resulted in lower rates, without much difference between MTE and Py complexes.

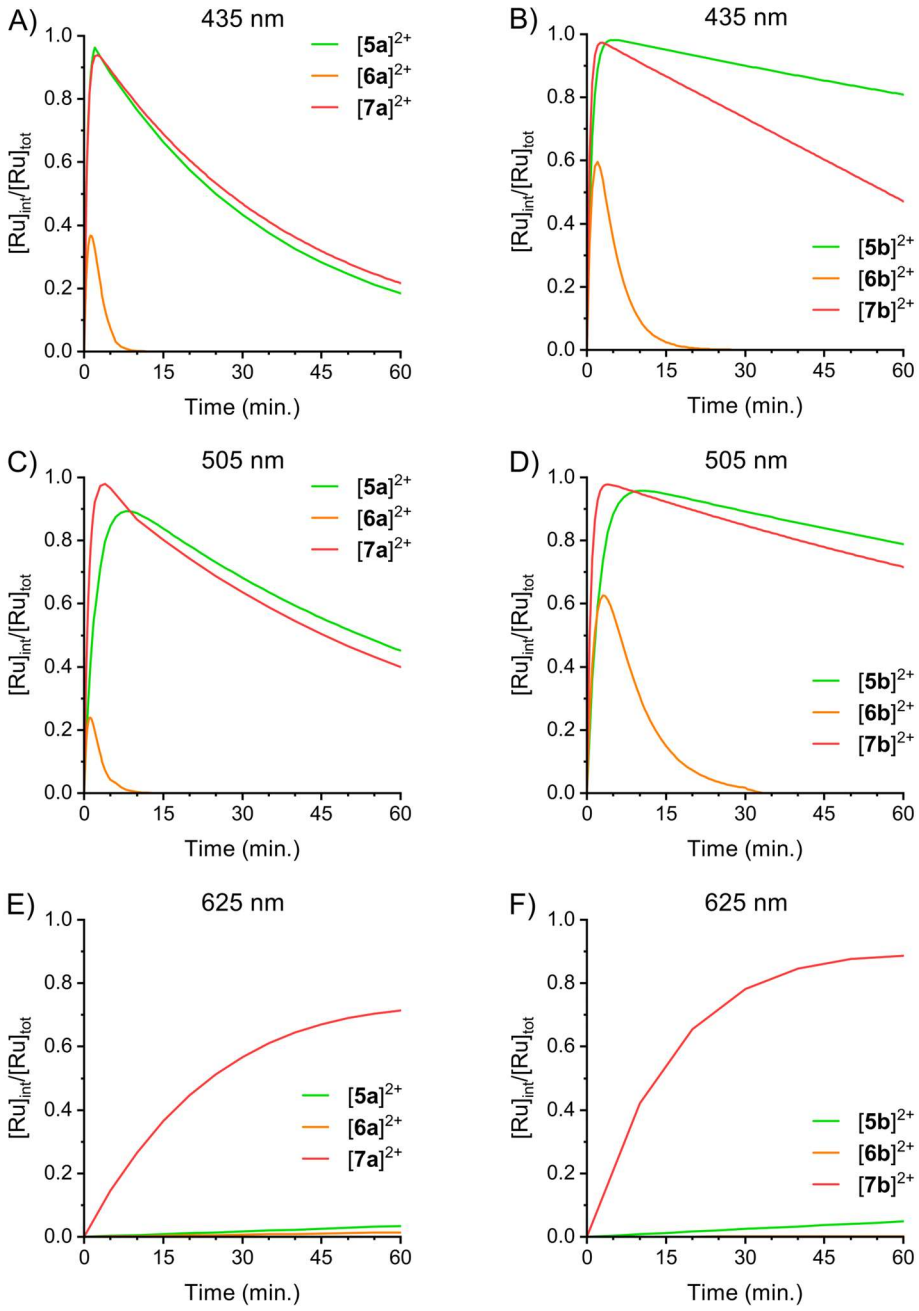

Figure 3.4 Kinetic curves obtained with global fitting of the absorbance spectra of [**1a,b**]$(PF_6)_2$ – [**3a,b**]$(PF_6)_2$ in 1/5 acetone/water at 298 K irradiated with blue (435 nm; A, B), green (505 nm; C, D), or red (625 nm) light, following the fraction of the intermediate species [**5a,b**]$^{2+}$ – [**7a,b**]$^{2+}$ ($[Ru]_{int}$) over the total ruthenium concentration ($[Ru]_{tot}$).

From these global fitted data and used photon fluxes it was also possible to calculate the photosubstitution quantum yields φ_1 and φ_2 for both steps of all complexes [**1a**,**b**]$^{2+}$ – [**3a**,**b**]$^{2+}$ (see Appendix III and Table 3.2). The QYs of the first photosubstitution step (φ_1) were found to be generally 2 orders of magnitude higher than the QY of the second step (φ_2). A notable exception was [**2a**]$^{2+}$, for which φ_2 was higher than φ_1 upon irradiation with either blue or green light. Irradiation with red light, which resulted in photoreactivity only for the Py complexes [**3a**]$^{2+}$ and [**3b**]$^{2+}$, gave $\varphi_{1,625}$ values of 0.0073 and 0.015, respectively. When comparing complexes containing **HL**, [**1a**]$^{2+}$ – [**3a**]$^{2+}$, with the ones containing **MeL**, [**1b**]$^{2+}$ – [**3b**]$^{2+}$, we noticed that the former compound showed QYs within the same order of magnitude with blue (435 nm) or green (505 nm) light. Surprisingly, the photoreactivity of the **MeL** complexes was much more dependent on the irradiation wavelength. For example, $\varphi_{1,435}$ and $\varphi_{1,505}$ are near-identical for [**1a**]$^{2+}$ (between 0.017 and 0.014, respectively), while the QYs for [**1b**]$^{2+}$ differed 5–fold ($\varphi_{1,435} = 0.079$ and $\varphi_{1,505} = 0.015$).

Table 3.2 Photochemical properties of [**1a**,**b**]$(PF_6)_2$ – [**3a**,**b**]$(PF_6)_2$ in 1/5 acetone/water at 298 K including maximum absorption wavelength (λ_{max}, in nm), molar extinction coefficient at the absorption maximum (ε_{max}, in $M^{-1}cm^{-1}$), molar extinction coefficient at irradiation wavelength for each step (ε_1 (λ_i), ε_2 (λ_i), in $M^{-1}cm^{-1}$) photosubstitution quantum yields (φ_1, φ_2) and photoreactivity at irradiation wavelength (ζ_1, ζ_2, in $M^{-1}cm^{-1}$).[a]

		[**1a**]$^{2+}$	[**1b**]$^{2+}$	[**2a**]$^{2+}$	[**2b**]$^{2+}$	[**3a**]$^{2+}$	[**3b**]$^{2+}$
	λ_{max} (nm) (ε_{max})[b]	439 (5300)	447 (6250)	429 (6990)	434 (6490)	486 (7200)	485 (6870)
435 nm	ε_1 (λ_i)[b]	5190	5450	6630	6480	3060	1960
	ε_2 (λ_i)[c]	4100	3800	4300	2600	3000	2400
	φ_1 (ζ_1)	0.017 (91)	0.079 (430)	0.032 (210)	0.034 (220)	0.018 (54)	0.19 (372)
	φ_2 (ζ_2)	0.00031 (1.3)	0.00029 (1.1)	0.041 (180)	0.020 (52)	0.00027 (0.82)	0.00083 (2.0)
505 nm	ε_1 (λ_i)[b]	1340	1190	1150	693	4140	4410
	ε_2 (λ_i)[c]	2500	2800	2000	1500	7000	5900
	φ_1 (ζ_1)	0.014 (18)	0.015 (18)	0.023 (27)	0.062 (43)	0.019 (77)	0.025 (110)
	φ_2 (ζ_2)	0.00023 (0.58)	0.00014 (0.39)	0.031 (63)	0.0098 (19)	0.00018 (0.54)	0.00019 (1.1)
625 nm	ε_1 (λ_i)[b]	226	36.3	82.6	6.03	82	42.2
	ε_2 (λ_i)[c]	520	140	290	6.4	460	440
	φ_1 (ζ_1)	0.00004 (0.009)	0.00035 (0.013)	0.00004 (0.0033)	0.00010 (0.0006)	0.0073 (0.60)	0.015 (0.65)
	φ_2 (ζ_2)	n.d. (<0.0052)	n.d. (<0.0013)	n.d. (<0.0029)	n.d. (<0.00008)	0.00016 (0.012)	0.00005 (0.02)

[a] $\zeta_i = \varepsilon(\lambda_i) \times \varphi_i$. [b] Molar extinction coefficient determined experimentally. [c] Molar extinction coefficient determined by global fitting.

For the dissymmetric complex [**4b**]$^{2+}$, the presence of two different monodentate ligands in axial positions, pyridine and an MTE, generates two possible intermediates [**7b**]$^{2+}$ and [**5b**]$^{2+}$ through via photosubstitution of either MTE ($\varphi_{1,S}$) or pyridine ($\varphi_{1,N}$), respectively (Scheme 3.4). The secondary photosubstitution, which can take place on each intermediate, leads to final bis-aqua complex [**8b**]$^{2+}$, by substitution of pyridine from [**7b**]$^{2+}$ ($\varphi_{2,N}$) or MTE from

[**5b**]$^{2+}$ ($\varphi_{2,S}$). For this complex there are hence 4 different photosubstitution reactions that may take place simultaneously upon light irradiation.

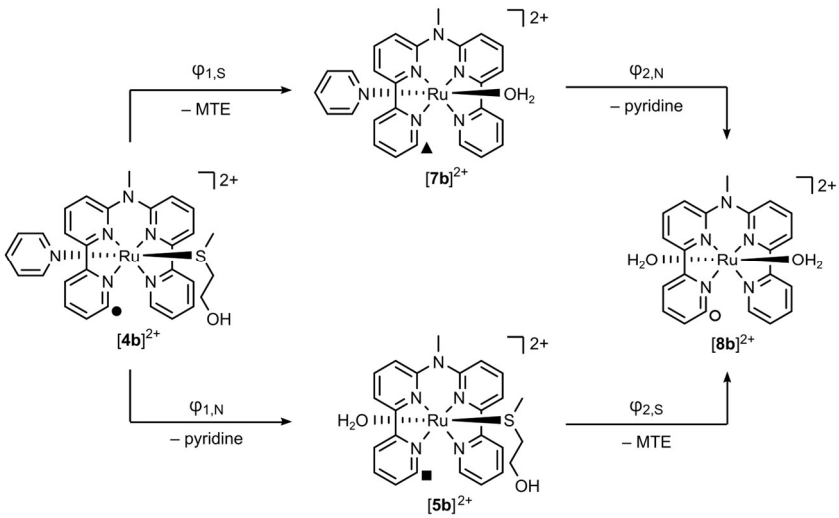

Scheme 3.4 Schematic overview of the possible photosubstitution pathways of [**4b**]$^{2+}$.

To investigate possible four photoreactions, a solution of [**4b**]$(PF_6)_2$ in 1/5 acetone-d_6/D_2O was initially monitored by ^{1}H-NMR upon irradiation, first using red light (650 nm) followed by green light (530 nm, Figure 3.5). Photorelease of axial ligands clearly took place, as indicated by the multiplet emerging at 8.39 ppm for free pyridine, the triplet appearing at 2.54 ppm for free MTE, and the disappearance of the doublet at 9.65 ppm of the starting reagent [**4b**]$^{2+}$. The time-evolution of the ratios of the integrals of the peaks corresponding to [**4b**]$^{2+}$ (9.5 - 9.8 ppm), free pyridine (8.2 - 8.4 ppm), and free MTE (2.5 - 3.2 ppm), divided by the integral of all ruthenium species, are presented in Figure 3.5B. These integral ratios indicated that after 6 h red light irradiation approximately half of [**4b**]$^{2+}$ had been converted: about half of the pyridine had been released while only 10% of MTE had been substituted. Subsequent irradiation with green light (530 nm) completed the conversion of [**4b**]$^{2+}$ by releasing of the residual pyridine within 1 h, while release of the remaining MTE required about 5 h irradiation at this wavelength and intensity. Clearly, red light irradiation of [**4b**]$^{2+}$ released primarily the pyridine ligand, while release of the thioether was slower and required more extensive green light irradiation. Etchenique et al. have reported selective photosubstitution of nitrogen-based ligands in *cis* ruthenium complexes containing also phosphine ligands that did not participate in the photosubstitution reactivity.[35] However, selective photosubstitution of pyridine in a ruthenium polypyridine complex containing two different photolabile ligands is, to our knowledge, unreported.

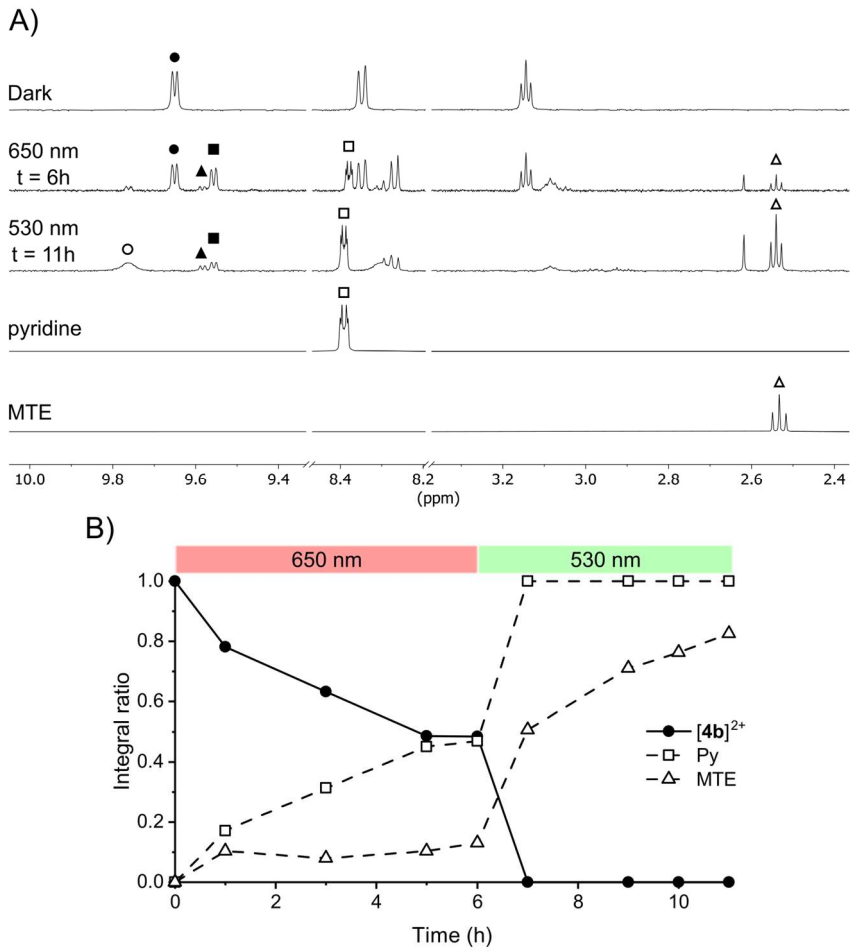

Figure 3.5 Sequential photosubstitution reactions of compound [**4b**]$^{2+}$ followed by ^{1}H-NMR. A) ^{1}H-NMR spectra of [**4b**]$(PF_6)_2$ (2.50 mM) measured in 1/5 acetone-d_6/D_2O before irradiation (dark), following 6 h irradiation with 650 nm light (~335 mW/cm^2), and finally following by a second step of 5 h irradiation with 530 nm light (~150 mW/cm^2). B) Time evolution of the ^{1}H-NMR integral ratios. As depicted in Scheme 3.4, the symbols indicate [**4b**]$^{2+}$ (●), intermediates [**5b**]$^{2+}$ (■) and [**7b**]$^{2+}$ (▲), photoproduct [**8b**]$^{2+}$ (○) free pyridine (Py, □) and free 2-(methylthio)ethanol (MTE, △).

The kinetics of the four photosubstitution reactions were investigated by recording the time evolution of the absorbance spectra of a solution of [**4b**]$(PF_6)_2$ in 1/5 acetone/H_2O at 298 K upon light irradiation with blue (435 nm), green (505 nm) or red light (625 nm). The spectra are shown in Figure 3.6. In all cases, the ^{1}MCLT band of the complex at 459 nm showed a bathochromic shift upon light irradiation. Interestingly, two isosbestic points at 414 nm and 470 nm were only observed upon red light irradiation, indicating the existence of a single photoreaction only when using low-energy light (Figure 3.6C). With blue or green light, clearly several photosubstitution reactions occurred simultaneously as indicated by the

absence of isosbestic points. However, when a solution first irradiated for 6 h with red light was subjected to a second irradiation using green light, another bathochromic shift with a single isosbestic point at 501 nm was also observed, indicating a second one-step photosubstitution reaction (Figure 3.6D). Since the UV-Vis absorbance spectra of [**5b**]$^{2+}$ and [**7b**]$^{2+}$ were obtained through global-fitting of the UV-Vis absorbance data from [**1b**]$^{2+}$ and [**3b**]$^{2+}$, respectively, the kinetics of the individual photoreactions starting from [**4b**]$^{2+}$ were deconvoluted through targeted-fitting (see Appendix I for details). Besides having an influence on the photosubstitution rates, the irradiation wavelength also influenced the ratio between the intermediates [**5b**]$^{2+}$ and [**7b**]$^{2+}$ present during the experiment (insets in Figure 3.6A-D). While a ratio of ~2 was found using green light irradiation, blue light irradiation resulted in an intermediate ratio of 10, confirming that in these *trans* complexes the photoreactivity strongly depended on the irradiation wavelength.

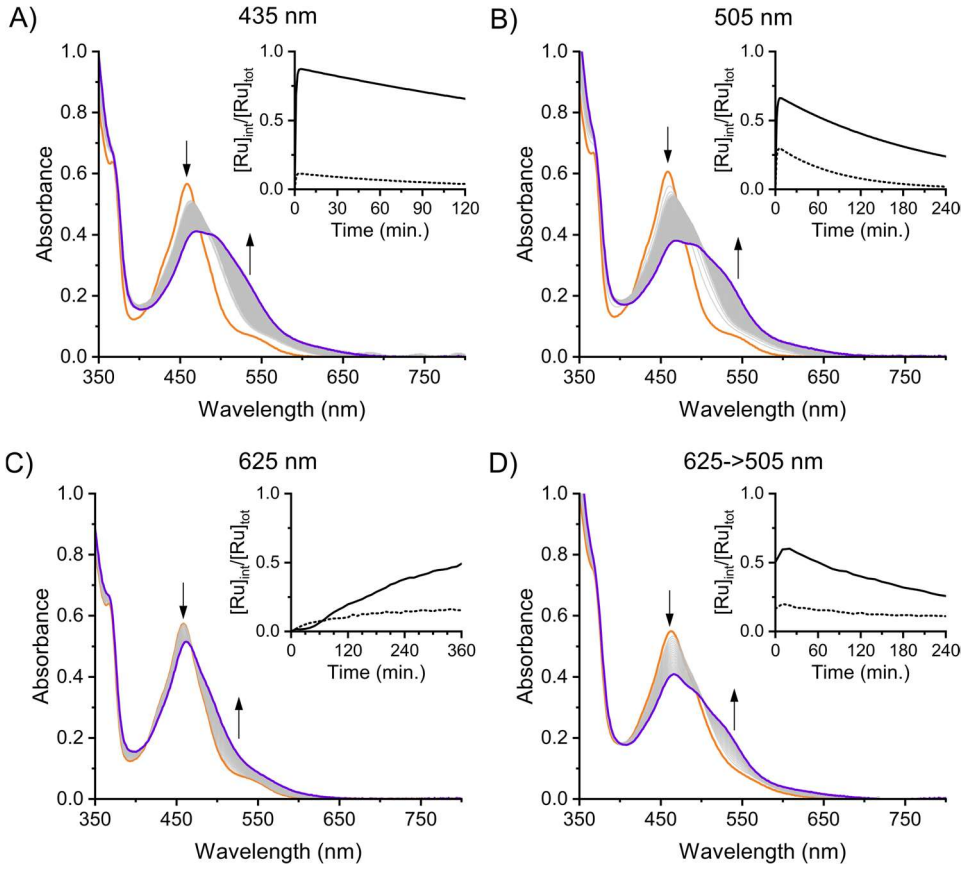

Figure 3.6 Time-evolution of the absorbance spectrum of a solution of [**4b**](PF$_6$)$_2$ in 1/5 acetone/water at 298 K irradiated with blue (435 nm, photon flux = 3.29 × 10^{-7} mol.s^{-1}; A), green (505 nm, photon flux = 2.00 × 10^{-7} mol.s^{-1}; B) or red (625 nm, photon flux = 4.24 × 10^{-7} mol.s^{-1}; C) light. In (D), the solution was irradiated first with red (625 nm) light for 6 h, then with green (505 nm) light after a 6 h period of

irradiation with red (625 nm) light. Inset depicts the evolution of the fraction of the two intermediates [**5b**]$^{2+}$ (solid line) and [**7b**]$^{2+}$ (dotted line) over the total ruthenium concentration $[Ru]_{tot}$ during irradiation.

To quantitatively analyze the kinetics of the photoreactivity of [**4b**]$(PF_6)_2$, the quantum yields of the four individual photosubstitution reactions were calculated using the targeted fitted data. The results are shown in Table 3.3. Most importantly, under blue light irradiation the photosubstitution of MTE ($\varphi_{1,S}$) proceeded with a quantum yield of 0.0017 while the quantum yield for pyridine substitution ($\varphi_{1,N}$) was almost one order of magnitude higher, i.e., 0.013. Similar differences in QY were also observed upon irradiation with green or red light. This selectivity towards Py substitution is in accordance with the preferred formation of intermediate [**5b**]$^{2+}$ observed in the ^{1}H-NMR experiments under light irradiation (as shown in Figure 3.5 and 3.6). Although $\varphi_{1,N}$ was mostly independent from the irradiation wavelength, distinct differences in QY were observed for $\varphi_{1,S}$: a much lower value (0.0017) was found upon 435 nm irradiation than for 505 nm irradiation (0.0085). Photosubstitution of the second ligand ($\varphi_{2,S}$ or $\varphi_{2,N}$) showed much lower QYs than that of the first ligand ($\varphi_{1,S}$ or $\varphi_{1,N}$), similar as observed for symmetrical complexes [**1b**]$^{2+}$ and [**3b**]$^{2+}$. For example, upon blue light irradiation $\varphi_{2,N}$ was 0.00074 and $\varphi_{2,S}$ was 0.000048, compared with 0.0017 and 0.013 for $\varphi_{1,S}$ and $\varphi_{1,N}$, respectively. Overall, these data highlighted a highly ligand-dependent and wavelength-dependent photosubstitution quantum efficiency for this complex as well.

Table 3.3 Photosubstitution properties for Steps 1 and 2 of [**4b**]$(PF_6)_2$ in 1/5 acetone/water at 298 K upon irradiation with blue (435 nm), green (505 nm) or red (625 nm) light including molar extinction coefficient ($\varepsilon(\lambda_{irr})$, in $M^{-1}cm^{-1}$), photosubstitution quantum yield (φ_i) and photoreactivity (ζ_i, in $M^{-1}cm^{-1}$) at irradiation wavelength.[a]

		$\varphi_{1,S}$ [b] ([**4b**]$^{2+}$ → [**7b**]$^{2+}$)	$\varphi_{1,N}$ [b] ([**4b**]$^{2+}$ → [**5b**]$^{2+}$)	$\varphi_{2,N}$ [c] ([**7b**]$^{2+}$ → [**8b**]$^{2+}$)	$\varphi_{2,S}$ [c] ([**5b**]$^{2+}$ → [**8b**]$^{2+}$)
435 nm	$\varepsilon(\lambda_i)$	4540	4540	3800	2400
	φ_i	0.0017	0.013	0.00074	0.000048
	(ζ_i)	(7.9)	(61)	(1.7)	(0.18)
505 nm	$\varepsilon(\lambda_i)$	1700	1700	2800	5900
	φ_i	0.0085	0.019	0.00035	0.00030
	(ζ_i)	(14)	(32)	(2.0)	(0.84)
625 nm	$\varepsilon(\lambda_i)$	3.26	3.26	140	440
	φ_i	0.0033	0.014	0.000030	0.000037
	(ζ_i)	(0.011)	(0.046)	(0.013)	(0.005)

[a] $\zeta_i = \varepsilon(\lambda_i) \times \varphi_i$. [b] Molar extinction coefficient determined experimentally. [c] Molar extinction coefficient determined by global fitting.

3.3 Discussion

The reactivity of ruthenium compounds towards photosubstitution is dependent on many electronic and structural aspects of a ruthenium(II) polypyridyl complex including the efficiency of absorbance of irradiation, steric repulsion towards the leaving ligand and stabilization of excited states. Of all the complexes reported here, only [**3b**]$^{2+}$, [**4b**]$^{2+}$ and to some extent [**3a**]$^{2+}$ were shown to undergo significant ligand photosubstitution upon red light (625 nm) irradiation even though their red-light absorbance was relatively low ($\varepsilon_{600\text{-}700}$ < 200 $M^{-1}cm^{-1}$). In contrast, photosubstitution was not detected for previously reported *trans* bis-pyridine ruthenium(II) complexes such as [Ru(qtpy)$(Py)_2$]$^{2+}$ (qtpy = 2,2':6',2":6",2"'-quaterpyridine) upon irradiation with blue light (470 nm) in water for 9 hours.[36] The red light photoreactivity of [**3b**]$^{2+}$, [**4b**]$^{2+}$ and [**3a**]$^{2+}$ must therefore be primarily induced by the tetrapyridyl ligands HL and MeL. Still, the presence of Py is of importance since MTE and ACN show minimal red light photoreactivity. Although Py is not causing the photoreactivity, it is the most labile for photosubstitution upon red light irradiation. The main difference between the qtpy and MeL complexes is that qtpy only generates 5-membered rings upon coordination to Ru, while MeL also generates a 6-membered ring involving the bridging amine. The difference in structure appears to have major consequences on the stability of the MLCT states, although such consequences should be confirmed by an extensive computational study. Whatever the reason, the ability to undergo photosubstitution reactions under red light irradiation is a strong advantage of complexes containing the MeL ligand, notably in the field of photoactivated chemotherapy where red light reactivity is often considered as prerequisite for clinical applications.

This being said, it is also interesting to discuss the wavelength dependence of pyridine *vs.* thioether photosubstitution, notably in [**4b**]$^{2+}$. The distinct photolability of Py and thioethers has been qualitatively observed in the *cis*-[Ru$(bpy)_2$(mtmp)]$^{2+}$, where the bidentate N,S-ligand 2-methylthiomethylpyridine (mtmp) was photosubstituted upon blue light irradiation.[37] While a sequential two-step process was clearly observed, a detailed photosubstitution mechanism was not reported and in particular it remained unclear if the thioether or pyridine was photosubstituted first. In this complex, the chelating nature of mtmp also forced a *cis* geometry of both ligands, while in [**4b**]$^{2+}$ they are *trans*. This new geometry, in combination with the availability of kinetic data for [**1b**]$^{2+}$, [**3b**]$^{2+}$, and [**4b**]$^{2+}$, allowed us to investigate for the first time *trans* effects in the excited state of metal compounds(Table 3.3).

Table 3.3 Substitution photoreactivities (ζ in $M^{-1}cm^{-1}$) of pyridine and MTE depending on the *trans* ligand upon irradiation with blue, green or red light.

	trans to / Ligand	Pyridine	MTE	OH_2
435 nm	Pyridine	372	61	2.0
	MTE	7.9	430	1.1
505 nm	Pyridine	110	32	1.1
	MTE	14	18	0.39
625 nm	Pyridine	0.65	0.046	0.02
	MTE	0.011	0.00035	<0.0013

According to our new, quantitative data, the *trans* effect in the excited state appears to be dependent on the wavelength of the light used for excitation. Under green light irradiation, the Py *trans* to MTE is almost four–fold less reactive towards photosubstitution compared to Py *trans* to Py ($\zeta_{1,N}$ = 32 in [**4b**]$^{2+}$ and ζ_1 = 110 in [**3b**]$^{2+}$, respectively). This difference increases to 14–fold when irradiated with red light ($\zeta_{1,N}$ = 0.046 in [**4b**]$^{2+}$ and ζ_1 = 0.65 in [**3b**]$^{2+}$), clearly indicating irradiation wavelength dependency. As the substitution reaction only occurs upon irradiation, the difference in reactivity is expected to originate from the properties of the excited states. This is supported by the near identical bond distances between the Ru(II) center and the axial ligands observed in the crystal structures of [**4b**]$(PF_6)_2$, [**1b**]$(PF_6)_2$ and [**3b**]$(PF_6)_2$, showing no significant *trans*-influence in the ground state. However, excitation of polypyridyl ruthenium(II) complexes leads, after intersystem crossing, to population of a triplet Metal-to-Ligand Charge Transfer excited state (^{3}MLCT). In this state, the polypyridyl ligand acquires a radical anion character while the metal center is formally oxidized to Ru(III), which increases interaction with σ- and π-donating ligands, while reducing the ability of the metal center to back-donate electron density into empty π* orbitals.[38] Thioethers are slightly σ- and π-donating ligands while pyridine is a strong σ-donating and good π-accepting ligand. In the ^{3}MLCT state of complex [**4b**]$^{2+}$, elongation of the Ru-Py bond is to be expected, increasing the ^{3}MLCT state energy. This results in a decrease in the energy gap between the ^{3}MLCT state and the triplet Metal-Centered excited state (^{3}MC), which is the more readily thermally accessible through intersystem crossing leading to ligand dissociation. However, compared to the symmetric bis-Py complex [**3b**]$^{2+}$, π-donation from MTE to the metal center in [**4b**]$^{2+}$ stabilizes the ^{3}MLCT state by enabling π-back-donation to Py. Consistent with this interpretation, Py photosubstitution occurs more efficiently in [**3b**]$^{2+}$ than in [**4b**]$^{2+}$.

Although φ_{PS} measurements at different wavelengths are rarely reported, the photosubstitution reactivity of ruthenium compounds is generally independent on excitation wavelength. For example, photosubstitution of the thioether ligand from $[Ru(tpy)(bpy)(R\text{-}SCH_3)]^{2+}$ has been reported with a quantum yield of 0.0055 with blue (445 nm) light and 0.0038 with green (530 nm) light in acetonitrile.[9] However, wavelength-dependent φ_{PS} for the photosubstitution of L from $[Ru(NH_3)_5(L)]^{2+}$ (where L is N-methylpyrazinium, isonicotinamide, pyrazine or 4-acetylpyridine) has been observed in aqueous solution.[39] For chromium complexes this wavelength-dependent effect on photosubstitution and excited-state dynamics has been revealed through transient absorbance spectroscopy.[40,41] A more recent, detailed study on the photophysics of a series of binuclear d^8d^8 di-isocyanide complexes with either Rh(I) or Ir(I), revealed specific relaxation cascades depending on the excitation wavelength.[42] For the symmetrical complexes reported here, excitation-wavelength dependency was only observed for **MeL** complexes [**1b**]$^{2+}$–[**3b**]$^{2+}$, with increasing φ_{PS} between 2- and 6-fold upon blue light irradiation compared to green or red light depending on the axial ligands. While the available data does not provide clear evidence for a specific photophysical mechanism, the correlation between φ_{PS} and excitation wavelength suggests more efficient population of the ^{3}MC state from higher $MLCT_n$ states, leading to more efficient photosubstitution (Figure 3.7). Since this effect is not observed for the **HL** complexes [**1a**]$^{2+}$–[**3a**]$^{2+}$, the **MeL** ligand possibly stabilizes MLCT states through its increased electron-donating character and rigidity, allowing for direct population of the ^{3}MC state from higher $^3MLCT_n$ states. While this photophysical mechanism remains a hypothesis, time-resolved spectroscopy combined with density-functional theory might provide more insight.

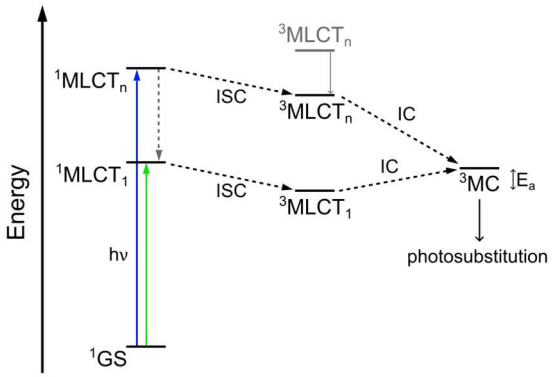

Figure 3.7 Proposed Jablonksi diagram for the excited state energy levels that are involved during photosubstitution of axial ligands from the **MeL** containing complexes [**1b**]$^{2+}$–[**3b**]$^{2+}$. Upon green light irradiation, the energetically lowest singlet Metal-to-Ligand-Charge-Transfer state ($^1MLCT_1$) is populated that, after intersystem crossing (ISC), converts to the $^3MLCT_1$ state and finally the dissociative triplet Metal-Centered state (^{3}MC) via internal conversion (IC). Excitation with blue light to higher $^1MLCT_n$ states however, can lead to population of $^3MLCT_n$ states that are accessible and can

directly convert to the ^{3}MC state. As the IC from ^{3}MLCT$_1$ to the ^{3}MC occurs thermally, an energy barrier (E_a) has to be overcome. This is not the case from the ^{3}MLCT$_n$ states as the conversion is energetically favorable, which leads to more efficient photosubstitution.

3.4 Conclusion

In this work, we successfully synthesized a series of *trans* ruthenium(II) complexes based on the tetrapyridyl ligand **HL** ([**1a**]$^{2+}$ – [**3a**]$^{2+}$) and its *N*-methyl analogue **MeL** ([**1b**]$^{2+}$ – [**3b**]$^{2+}$). This ligand occupies the basal plane of an octahedron, leaving two *trans* axial positions for the coordination of monodentate ligands L' and L" such as thioethers (MTE), acetonitrile (ACN), and pyridine (Py), resulting in symmetrical complexes [**1a,b**]$^{2+}$ – [**3a,b**]$^{2+}$ (L'=L"). Additionally, dissymmetric complex [**4b**]$^{2+}$ containing both MTE and Py as axial ligands (L'≠L"), was prepared by red light irradiation (650 nm) of [**3b**]$^{2+}$ in presence of MTE. The crystal structure of [**4b**]$^{2+}$ did not reveal significant differences in bond distances, angles or geometrical distortion compared to symmetric complexes [**1b**]$^{2+}$ and [**3b**]$^{2+}$, suggesting the absence of a *trans* influence in the ground state. The photochemical properties of the complexes were characterized by UV-Vis absorbance and ^{1}H-NMR spectrometry, which revealed significant differences in photoreactivity. For the ACN complexes [**2a,b**]$^{2+}$, both substitution reactions occurred with similar rates when irradiated with blue (435 nm) or green (505 nm) light in 1/5 acetone/H_2O. In contrast, substitution of the second MTE in [**1a,b**]$^{2+}$ and pyridine in [**3a,b**]$^{2+}$ occurred much less efficient than the first one in the same conditions. For the symmetrical complexes, red light (625 nm) irradiation only resulted in photosubstitution of the axial ligands in bis-Py complexes [**3a,b**]$^{2+}$. Interestingly, the **MeL** containing complexes [**1**–**3b**]$^{2+}$ showed higher photosubstitution quantum yields upon blue light irradiation than for green or red light, indicating excitation-wavelength dependency of the quantum efficiency of the photoreaction.

Visible-light induced photosubstitution of both MTE and Py ligands in [**4b**]$^{2+}$, was shown to proceed to the bis-aqua photoproduct [**8b**]$^{2+}$ via the formation of intermediates [**5b**]$^{2+}$ (L'=MTE; L"=OH_2) as well as [**7b**]$^{2+}$ (L'=OH_2; L"=Py). Targeted fitting of the time-evolution UV-Vis absorbance data, allowed for the determination of the photosubstitution quantum yields of each individual step. While photosubstitution of both ligands was observed with blue or green light, the kinetic data revealed selectivity towards Py over MTE substitution from [**4b**]$^{2+}$, depending on the irradiation wavelength. Strikingly, red light (625 nm) irradiation resulted in a 4-fold increase in Py photosubstitution quantum yield. The wavelength-dependent photosubstitution selectivity of [**4b**]$^{2+}$ enabled for sequential release of pyridine with red light, followed by MTE release with green light. These first-in-class results open unprecedented opportunities in the field of photoactivated chemotherapy, where two inhibitors based on thioether and pyridine may be released sequentially using light of different color.

3.5 Experimental

3.5.1 General information

Unless otherwise noted, all reagents and solvents were purchased from commercial suppliers (Fluorochem, Sigma-Aldrich, BLDPharm, VWR, TCI) and used without further purification. [2,2'-bipyridine]-6-amine was synthesized according to the procedure reported in Chapter 2.[43] Anhydrous and oxygen-free solvents were obtained using common distillation, drying (activated 4 Å molecular sieves) and degassing (freeze-pump-thaw method) procedures. The reactions were carried under air unless stated otherwise. The standard Schlenk technique was used for the reactions that were carried out under nitrogen atmosphere. Filters used were Whatman® regenerated cellulose membrane filters, RC60 Membrane circles, diam. 47 mm, pore size 1 µm. TLCs were performed using either Supelco analytical silica gel on Al foils with fluorescence indicator 254 nm or Supelco analytical aluminum oxide 60 with fluorescence indicator 254 nm. Column chromatography was carried on silica gel (40-63 µm) or on activated neutral aluminum oxide (Brockmann Grade I) from VWR Chemicals. The microwave tubes (product number: 351521) were purchased from Biotage (Uppsala, Sweden) and heated using Thermo Scientific™ Reacti-block™ T-1 (9 holes; dimensions: 17mm diameter × 45 mm deep). All synthesized ruthenium complexes were stored at room temperature and protected from light. NMR spectra were recorded on Bruker Avance 300, 400 or 500 MHz and the FIDs were treated with MestReNova software. The chemical shifts are given relative to the residual signal of the solvent (Acetone-d6: δ (^{1}H) = 2.05 ppm, δ (^{13}C) = 29.84 ppm; $CDCl_3$: δ (^{1}H) = 7.26 ppm, δ (^{13}C) = 77.16 ppm; DMSO-d6: δ (^{1}H) = 2.50 ppm, δ (^{13}C) = 39.52 ppm), or relative to an external standard (TMS: δ (^{1}H) = 0 ppm, δ (^{13}C) = 0 ppm). The mass spectra were recorded in methanol (UPLC grade) with 1% (v/v) of formic acid on a Shimadzu LCMS-2020 (ESI-Q). The high-resolution mass spectra (HRMS) were recorded on a Thermo Finnigan LTQ Orbitrap.

3.5.2 Synthesis

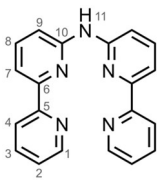

di([2,2'-bipyridin]-6-yl)amine, HL: In a 250 mL two-necked flask was transferred 6-bromo-2,2'-bipyridine (3.32 g, 14.02 mmol, 1.0 eq), [2,2'-bipyridine]-6-amine (2.42 g, 14.02 mmol, 1.0 eq), palladium bis(dibenzylideneacetone) (660 mg, 1.121 mmol, 0.08 eq), 1,3-bis(diphenylphosphino)propane (469 mg, 1.121 mmol, 0.08 eq) and sodium tert-butoxide (1.905 g, 19.63 mmol, 1.4 eq). The flask was purged with nitrogen by cycling three times between vacuum and nitrogen. After 140 mL of toluene, the mixture was stirred at 80 °C and the reaction progress was followed by TLC (Alumina; 1 : 1 EtOAc : toluene). Once the amine and bromide starting materials were both consumed (after 22 h), the mixture was allowed to cool to RT. 50 mL of H2O was added and stirred for 1 hour. The layers were separated and the aqueous phase was extracted with DCM (3 x 200

mL). The combined organic layers were washed with brine (200 mL), dried with $MgSO_4$ and concentrated in vacuo. The resulting crude was purified by column chromatography (Alumina; 10 − 40% EtOAc : toluene) yielding the target compound as an off-white powder (4.33 g, 13.3 mmol, 95%). Analysis was consistent with previous reports.[26] ^{1}H NMR (400 MHz, DMSO-d6) δ 9.91 (s, 1H, H^{11}), 8.69 (ddd, J = 4.8, 1.8, 0.9 Hz, 2H, H^1), 8.38 (dt, J = 7.9, 1.1 Hz, 2H, H^4), 8.01 – 7.96 (m, 2H, H^3), 7.95 – 7.85 (m, 6H, H^7, H^8, H^9), 7.45 (ddd, J = 7.5, 4.7, 1.2 Hz, 2H, H^2). ^{13}C{^{1}H} NMR (101 MHz, DMSO-d6) δ 155.47 (C^5), 153.86 (C^{10}), 153.43 (C^6), 149.29 (C^1), 138.74 (C^7, C^8, C^9), 137.28 (C^3), 124.00 (C^2), 120.38 (C^4), 112.84 (C^7, C^8, C^9), 112.32 (C^7, C^8, C^9). ESI-MS: exact m/z calculated for $[C_{20}H_{15}N_5 + H^+]^+$: 326.1 m/z, found: 326.2 m/z.

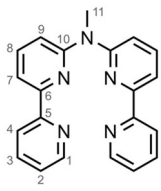

***N*-bis([2,2'-bipyridin]-6-yl)-N-methylamine**, **MeL**: Potassium hydroxide (3.45 g, 61.5 mmol, 10 eq) was added to a solution of di([2,2'-bipyridin]-6-yl)amine **L** (2.0 g, 6.15 mmol, 1.0 eq) in 60 mL DMSO and the mixture was stirred at RT. After 1.5 hours, iodomethane (2.3 mL, d = 0.461 g/mL, 7.38 mmol, 1.2 eq) was added and stirred for another 2 hours. The reaction was quenched with 150 mL H2O and extracted with toluene (5 x 150 mL). The combined organic phase was dried with $MgSO_4$ and concentrated in vacuo. Purified by flash column chromatography (Alumina; 10 – 50% EtOAc : Toluene + 0.5% Et_3N) yielded the product as an off-white powder (1.78 g, 5.26 mmol, 85%). Analysis was consistent with previous reports.[44] ^{1}H NMR (400 MHz, DMSO-d6) δ 8.68 (ddd, *J* = 4.8, 1.8, 0.9 Hz, 2H, H^1), 8.31 (dt, J = 8.0, 1.1 Hz, 2H, H^4), 8.00 (dd, *J* = 7.5, 0.8 Hz, 2H, H^7), 7.94 (td, *J* = 7.7, 1.8 Hz, 2H, H^3), 7.86 (dd, *J* = 8.3, 7.5 Hz, 2H, H^8), 7.46 – 7.39 (m, 4H, H^2, H^9), 3.75 (s, 3H, H^{11}). ^{13}C{^{1}H} NMR (101 MHz, DMSO-d6) δ 156.48 (C^{10}), 155.29 (C^5), 153.47 (C^6), 149.25 (C^1), 138.59 (C^8), 137.30 (C^3), 124.08 (C^2), 120.38 (C^4), 114.59 (C^9), 113.67 (C^7), 35.67 (C^{11}). ESI-MS: exact m/z calculated for $[C_{21}H_{17}N_5 + H^+]^+$: 340.2 m/z, found: 340.2 m/z.

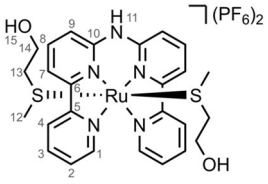

[Ru(L)(MTE)$_2$](PF$_6$)$_2$, [**1a**](PF$_6$)$_2$: To a 50 mL two-necked flask was added **L** (100 mg, 0.31 mmol, 1 eq), $Ru(DMSO)_4Cl_2$ (150 mg, 0.31 mmol, 1 eq) and the flask was purged with nitrogen by cycling three times between vacuum and nitrogen. After addition of 2-(methylthio)ethanol (8.0 mL, d = 1.06 g/mL, 92 mmol), the mixture was stirred at 150 °C while monitoring the reaction progress by TLC (SiO_2; acetone : H_2O : aq. saturated KPF_6, 10 : 1 : 1). After 72 hours, the mixture was cooled to RT and precipitated in a 100 mL half saturated aqueous KPF_6 solution. The precipitate was filtered over a membrane filter and washed with a minimal amount of half saturated aqueous KPF_6 followed by diethyl ether. Drying under high vacuum yielded the product as a

brown powder (196 mg, 0.22 mmol, 71%). Brown/red single crystals suitable for X-ray diffraction were obtained using vapor diffusion of diethyl ether into a solution of [**1a**]$(PF_6)_2$ in 1:1 THF/acetone. ^{1}H NMR (500 MHz, Acetone-d_6) δ 11.38 (s, 1H, H^{11}), 9.92 (ddd, *J* = 5.7, 1.4, 0.7 Hz, 2H, H^1), 8.96 (dt, *J* = 8.2, 1.1 Hz, 2H, H^4), 8.63 (dd, *J* = 7.9, 0.9 Hz, 2H, H^7), 8.45 (ddd, *J* = 8.1, 7.5, 1.4 Hz, 2H, H^3), 8.38 (dd, *J* = 8.4, 7.7 Hz, 2H, H^8), 8.07 (ddd, *J* = 7.4, 5.7, 1.4 Hz, 2H, H^2), 7.83 (dd, *J* = 8.4, 1.0 Hz, 2H, H^9), 3.75 (t, *J* = 5.2 Hz, 2H, H^{15}), 3.28 (q, *J* = 5.6 Hz, 4H, H^{14}), 1.77 (t, *J* = 5.8 Hz, 4H, H^{13}), 1.34 (s, 6H, H^{12}). ^{13}C{H} NMR (126 MHz, Acetone-d_6) δ 158.35 (C^{10}), 156.04 (C^5), 154.69 (C^1), 150.27 (C^6), 139.87 (C^3), 138.94 (C^8), 128.36 (C^2), 125.40 (C^4), 118.91 (C^7), 117.45 (C^9), 59.00 (C^{14}), 37.91 (C^{13}), 16.00 (C^{12}). ESI-MS: exact m/z calculated for $[C_{26}H_{31}N_5O_2RuS_2]^{2+}$: 305.6 m/z, found: 305.3 m/z. Elemental analysis (%) for compound [**1a**]$(PF_6)_2$ ($C_{26}H_{31}F_{12}N_5O_2P_2RuS_2$), calculated C, 34.67; H, 3.47; N, 7.78; found C, 34.28; H, 3.41; N, 7.63. UV-Vis (1/5 H_2O/acetone): λ_{max} (ε): 440 nm (5.1×10^3 $M^{-1}cm^{-1}$).

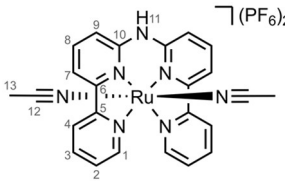

[Ru(L)(ACN)$_2$](PF$_6$)$_2$, [**2a**]$(PF_6)_2$: A solution of [**1a**]$(PF_6)_2$ (61 mg, 0.068 mmol, 1 eq) in ACN (6.5 mL, 0.10 M) was stirred at 80 °C under N_2. The conversion was monitored by TLC (SiO_2; acetone : H_2O : aq. saturated KPF_6, 10 : 1 : 1). After 5 days, the mixture was cooled to RT and precipitated in a 60 mL half saturated aqueous KPF_6 solution. The precipitate was filtered over a membrane filter and washed with a minimal amount of half saturated aqueous KPF_6 followed by diethyl ether. Drying under high vacuum yielded the product as a brown powder (43 mg, 0.054 mmol, 79%). ^{1}H NMR (500 MHz, Acetone-d_6) δ 11.30 (s, 1H, H^{11}), 9.88 (d, *J* = 5.6 Hz, 2H, H^1), 8.89 (d, *J* = 8.0 Hz, 2H, H^4), 8.55 (d, *J* = 8.0 Hz, 2H, H^7), 8.42 (td, *J* = 7.8, 1.4 Hz, 2H, H^3), 8.34 (t, *J* = 8.0 Hz, 2H, H^8), 8.02 (ddd, *J* = 7.3, 5.5, 1.4 Hz, 2H, H^2), 7.79 (dd, *J* = 8.4, 0.9 Hz, 2H, H^9), 1.98 (s, 6H, H^{13}). ^{13}C{H} NMR (126 MHz, Acetone-d_6) δ 158.74 (C^{10}), 156.75 (C^5), 154.55 (C^1), 150.63 (C^6), 139.62 (C^3), 138.94 (C^8), 127.58 (C^2), 125.71 (C^{12}), 124.52 (C^4), 117.80 (C^7), 116.66 (C^9), 3.28 (C^{13}). ESI-MS: exact m/z calculated for $[C_{24}H_{21}N_7Ru]^{2+}$: 254.5 m/z, found: 254.2 m/z and $[C_{24}H_{21}N_7Ru - H^+]^+$: 508.1 m/z, found: 508.0 m/z. Elemental analysis (%) for compound [**2a**]$(PF_6)_2$ ($C_{24}H_{21}F_{12}N_7P_2Ru$), calculated C, 36.10; H, 2.65; N, 12.28; found C, 35.18; H, 2.68; N, 11.91. UV-Vis (1/5 H_2O/acetone): λ_{max} (ε): 429 nm (7.0×10^3 $M^{-1}cm^{-1}$).

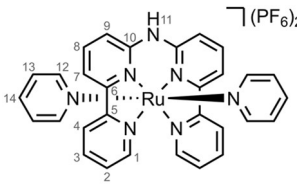

[Ru(L)(Py)$_2$](PF$_6$)$_2$, [**3a**]$(PF_6)_2$: A solution of [**1a**]$(PF_6)_2$ (55 mg, 0.061 mmol, 1 eq) in pyridine (6.0 mL, 0.10 M) was stirred at 115 °C under N_2. The conversion was monitored by TLC (SiO_2; acetone : H_2O : aq. saturated KPF_6, 10 : 1 : 1). After 24 hours, the mixture was cooled to RT and precipitated in a 60 mL half saturated aqueous KPF_6 solution. The precipitate was filtered over a membrane filter and washed with a minimal amount of half saturated aqueous KPF_6 followed by diethyl ether. Drying under high vacuum yielded the product as a red powder (50 mg, 0.054 mmol, 93%).

^{1}H NMR (500 MHz, DMSO-d_6) δ 12.35 (s, 1H, H^{11}), 9.97 (d, *J* = 6.2 Hz, 2H, H^1), 8.75 (d, *J* = 8.1 Hz, 2H, H^4), 8.45 (d, *J* = 7.7 Hz, 2H, H^7), 8.30 – 8.22 (m, 4H, H^3, H^8), 8.02 (ddd, *J* = 7.2, 5.6, 1.3 Hz, 2H, H^2), 7.85 (d, *J* = 8.4 Hz, 2H, H^9), 7.59 – 7.52 (m, 6H, H^{12}, H^{14}), 7.02 (dd, *J* = 8.1, 6.0 Hz, 4H, H^{13}). ^{13}C{H} NMR (126 MHz, DMSO-d_6) δ 156.85 (C^{10}), 154.77 (C^5), 153.32 (C^1), 151.85 (C^{12}), 148.47 (C^6), 138.32 (C^3), 137.57 (C^{14}), 137.03 (C^8), 127.35 (C^2), 125.76 (C^{13}), 123.71 (C^4), 117.39 (C^7), 116.61 (C^9). ESI-MS: exact m/z calculated for $[C_{30}H_{25}N_7Ru]^{2+}$: 292.6 m/z, found: 292.5 m/z and $[C_{30}H_{25}N_7Ru - H^+]^+$: 584.1 m/z, found: 584.2m/z. Elemental analysis (%) for compound [**3a**]$(PF_6)_2$ ($C_{30}H_{25}F_{12}N_7P_2Ru$), calculated C, 41.20; H, 2.88; N, 11.21; found C, 40.64; H, 2.91; N, 11.03. UV-Vis (1/5 H_2O/acetone): λ_{max} (ε): 486 nm (7.0×10^3 $M^{-1}cm^{-1}$).

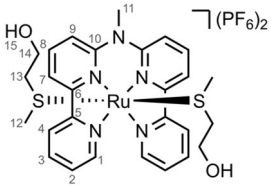

[Ru(MeL)(MTE)$_2$](PF$_6$)$_2$, [**1b**](PF$_6$)$_2$: To a 100 mL two-necked flask was added **MeL** (337 mg, 1 mmol, 1 eq), Ru(DMSO)$_4$Cl$_2$ (480 mg, 1 mmol, 1 eq) and the flask was purged with nitrogen by cycling three times between vacuum and nitrogen. After addition of 2-(methylthio)ethanol (2.2 mL, d = 1.06 g/mL, 25 mmol, 25 eq) and methanol (20 mL), the mixture was stirred at 150 °C while monitoring the reaction progress by TLC (SiO_2; acetone : H_2O : aq. saturated KPF_6, 10 : 1 : 1). After 48 hours, the mixture was cooled to RT and precipitated in a 100 mL half saturated aqueous KPF_6 solution. The precipitate was filtered over a membrane filter and washed with a minimal amount of half saturated aqueous KPF_6 followed by diethyl ether. Drying under high vacuum yielded the product as a brown-orange powder (823 mg, 0.90 mmol, 90%). Pale orange needle-shaped single crystals suitable for X-ray diffraction were obtained using vapor diffusion of diethyl ether into a solution of [**1b**](PF$_6$)$_2$ in acetone containing 5 molar equivalents of triphenylphosphine oxide. ^{1}H NMR (400 MHz, Acetone-d_6) δ 9.85 (ddd, *J* = 5.7, 1.6, 0.8 Hz, 2H, C^1), 8.92 (dt, *J* = 8.1, 1.1 Hz, 2H, C^4), 8.66 (dd, *J* = 7.9, 0.9 Hz, 2H, H^7), 8.47 – 8.37 (m, 4H, H^3, H^8), 8.08 – 7.99 (m, 4H, H^2, H^9), 4.22 (s, 3H, H^{11}), 3.75 (t, *J* = 5.2 Hz, 2H, H^{15}), 3.27 (q, *J* = 5.5 Hz, 4H, H^{14}), 1.80 (t, *J* = 5.8 Hz, 4H, H^{13}), 1.36 (s, 6H, H^{12}). ^{13}C{^{1}H} NMR (101 MHz, Acetone-d_6) δ 158.56 (C^{10}), 156.80 (C^5), 156.26 (C^6), 154.60 (C^1), 140.10 (C^3), 139.18 (C^8), 128.49 (C^2), 125.61 (C^4), 119.52 (C^7), 119.10 (C^9), 59.09 (C^{14}), 44.85 (C^{11}), 38.29 (C^{13}), 16.38 (C^{12}). ESI-MS: exact m/z calculated for $[C_{27}H_{33}N_5O_2RuS_2]^{2+}$: 312.6 m/z, found: 312.1 m/z. Elemental analysis (%) for compound [**1b**](PF$_6$)$_2$ ($C_{27}H_{33}F_{12}N_5O_2P_2RuS_2$), calculated C, 35.45; H, 3.64; N, 7.66; found C, 35.30; H, 3.68; N, 7.61. UV-Vis (1/5 H_2O/acetone): λ_{max} (ε): 447 nm (6.5×10^3 $M^{-1}cm^{-1}$).

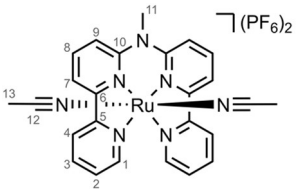

[Ru(MeL)(ACN)$_2$](PF$_6$)$_2$, [**2b**](PF$_6$)$_2$: [**1b**](PF$_6$)$_2$ (120 mg, 0.13 mmol, 1 eq) was added to an 8 mL microwave tube. The tube was sealed with a crimp cap and purged with nitrogen by cycling three times between vacuum and nitrogen. After addition of acetonitrile (1.31 mL, d = 0.786 g/mL, 25.0 mmol,

190 eq), the mixture was stirred at 80 °C while monitoring the reaction progress by TLC (SiO_2; acetone : H_2O : aq. saturated KPF_6, 8 : 1 : 1). After 48 hours, the mixture was cooled to RT and precipitated in a 100 mL half saturated aqueous KPF_6 solution. The precipitate was filtered over a membrane filter and washed with a minimal amount of half saturated aqueous KPF_6 followed by diethyl ether. Drying under high vacuum resulted the crude product. Further purification by column chromatography (SiO_2; acetone : H_2O : aq. saturated KPF_6, 8 : 1 : 1) yielded the pure product as an orange-brown powder (49 mg, 0.06 mmol, 46%). Orange single crystals suitable for X-ray diffraction were obtained using vapor diffusion of diethyl ether into a solution of [**2b**]$(PF_6)_2$ in acetone. ^{1}H NMR (400 MHz, Acetone-*d*$_6$) δ 9.81 (ddd, *J* = 5.6, 1.5, 0.7, 2H, H^1), 8.85 (dt, *J* = 8.2, 1.0 Hz, 2H, H^4), 8.57 (dd, *J* = 7.9, 0.9 Hz, 2H, H^7), 8.44 – 8.34 (m, 4H, H^3, H^8), 8.05 – 7.94 (m, 4H, H^2, H^9), 4.19 (s, 3H, H^{11}), 1.99 (s, 6H, H^{13}). ^{13}C{^{1}H} NMR (101 MHz, Acetone-*d*$_6$) δ 158.95 (C^{10}), 157.38 (C^5), 156.57 (C^6), 154.48 (C^1), 139.86 (C^3), 139.24 (C^8), 127.72 (C^2), 125.59 (C^{12}), 124.79 (C^4), 118.49 (C^7), 118.23 (C^9), 44.75 (C^{11}), 3.24 (C^{13}). ESI-MS: exact m/z calculated for $[C_{25}H_{23}N_7Ru]^{2+}$: 261.5 m/z, found: 261.2 m/z and $[C_{25}H_{23}N_7Ru + PF_6]^+$: 668.1 m/z, found: 668.0 m/z. Elemental analysis (%) for compound [**2b**]$(PF_6)_2$ ($C_{25}H_{23}F_{12}N_7P_2Ru$), calculated C, 36.96; H, 2.85; N, 12.07; found C, 36.78; H, 2.86; N, 11.97. UV-Vis (1/5 H_2O/acetone): λ_{max} (ε): 434 nm (6.5 × 10^3 $M^{-1}cm^{-1}$).

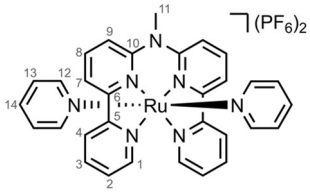

[Ru(MeL)(Py)$_2$](PF$_6$)$_2$, [**3b**]$(PF_6)_2$: [**1b**]$(PF_6)_2$ (250 mg, 0.273 mmol, 1 eq) was added to an 8 mL microwave tube. The tube was sealed with a crimp cap and with nitrogen by cycling three times between vacuum and nitrogen. After addition of pyridine (2.75 mL, d = 0.982 g/mL, 34.2 mmol, 125 eq), the mixture was stirred at 115 °C while monitoring the reaction progress by TLC (SiO_2; acetone : H_2O : aq. saturated KPF_6, 10 : 1 : 1). After 48 hours, the mixture was cooled to RT and precipitated in a 250 mL half saturated aqueous KPF_6 solution. The precipitate was filtered over a membrane filter and washed with a minimal amount of half saturated aqueous KPF_6 followed by diethyl ether. Drying under high vacuum yielded the product as a red powder (188 mg, 0.21 mmol, 77%). Red needle-shaped single crystals suitable for X-ray diffraction were obtained using vapor diffusion of diethyl ether into a solution of [**3b**]$(PF_6)_2$ in acetone. ^{1}H NMR (400 MHz, Acetone-*d*$_6$) δ 10.06 (d, *J* = 5.6 Hz, 2H, H^1), 8.73 (d, *J* = 8.1 Hz, 2H, H^4), 8.48 (d, *J* = 7.7 Hz, 2H, H^7), 8.32 (dt, *J* = 10.6, 7.8 Hz, 4H, H^3, H^8), 8.10 – 8.03 (m, 4H, H^2, H^9), 7.78 – 7.73 (m, 4H, H^{12}), 7.63 (dd, *J* = 8.5, 7.0 Hz, 2H, H^{14}), 7.02 (t, *J* = 6.9 Hz, 4H, H^{13}), 4.15 (s, 3H, H^{11}). ^{13}C{^{1}H} NMR (101 MHz, Acetone-*d*$_6$) δ 158.65 (C^{10}), 157.18 (C^5), 156.11 (C^6), 154.17 (C^1), 153.07 (C^{12}), 139.67 (C^3), 138.49 (C^8), 138.45 (C^{14}), 128.65 (C^2), 126.53 (C^{13}), 125.11 (C^4), 119.17 (C^7), 119.13 (C^9), 44.27 (C^{11}). ESI-MS: exact m/z calculated for $[C_{31}H_{27}N_7Ru]^{2+}$: 299.6 m/z, found: 299.5 m/z and $[C_{31}H_{27}N_7Ru + PF_6]^+$: 744.1 m/z, found: 744.1 m/z. Elemental analysis (%) for compound [**3b**]$(PF_6)_2$ ($C_{31}H_{27}F_{12}N_7P_2Ru$), calculated C,

41.90; H, 3.06; N, 11.03; found C, 41.58; H, 3.04; N, 10.97. UV-Vis (1/5 H_2O/acetone): λ_{max} (ε): 485 nm (7.1 × 10^3 $M^{-1}cm^{-1}$).

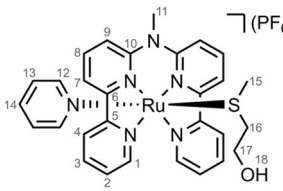

[Ru(MeL)(Py)(MTE)](PF$_6$)$_2$, [**4b**](PF$_6$)$_2$: [**3b**](PF$_6$)$_2$ (148 mg, 0.17 mmol, 1 eq) in 50 mL acetone and 17 mL of a 100 mM solution of 2-(methylthio)ethanol (1.7 mmol, 10 eq) in acetone were added under nitrogen to a 140 mL double-walled photoreactor with water cooling (see Figure I.1). Acetone was added to a total volume of 125 mL and the reaction mixture was irradiated with a 650 nm LED lamp at RT while monitoring the reaction progress by TLC (SiO_2; acetone : H_2O : aq. saturated KPF_6, 10 : 1 : 1). After 1 hour, the mixture was concentrated *in vacuo* and precipitated in diethyl ether. The precipitate was filtered over a membrane filter and washed with diethyl ether. The mixture was purified by column chromatography (SiO_2; acetone : H_2O : aq. saturated KPF_6, 8 : 1 : 1). The product containing fractions were combined and concentrated, followed by precipitation in 100 mL half saturated aqueous KPF_6. After filtration over a membrane filter, the product was washed with a minimal amount of water followed by diethyl ether. Drying under high vacuum yielded the product as an orange powder (95 mg, 0.10 mmol, 63%). Red/brown needle-shaped single crystals suitable for X-ray diffraction were obtained using vapor diffusion of diethyl ether into a solution of [**4b**](PF$_6$)$_2$ in acetone/THF (1:1). ^{1}H NMR (400 MHz, Acetone-*d*$_6$) δ 10.05 (ddd, *J* = 5.6, 1.5, 0.8 Hz, 2H, H^1), 8.70 (dt, *J* = 8.1, 1.2 Hz, 2H, H^4), 8.46 (dd, *J* = 7.8, 0.9 Hz, 2H, H^7), 8.31 – 8.31 (m, 4H, H^3, H^8), 8.13 – 8.04 (m, 4H, H^2, H^9), 7.73 – 7.68 (m, 2H, H^{12}), 7.60 (tt, *J* = 7.6, 1.5 Hz, 1H, H^{14}), 6.99 (dd, *J* = 7.6, 6.6 2H, H^{13}), 4.27 (s, 3H, H^{11}), 3.80 (t, *J* = 5.2 Hz, 1H, H^{18}), 3.37 (td, *J* = 5.8, 4.9 Hz, 2H, H^{17}), 1.59 (s, 3H, H^{15}). ^{13}C{^{1}H} NMR (101 MHz, Acetone-*d*$_6$) δ 158.47 (C^{10}), 156.90 (C^5), 156.20 (C^6), 154.38 (C^1), 151.82 (C^{12}), 139.89 (C^3), 139.22 (C^{14}), 138.94 (C^8), 128.69 (C^2), 126.82 (C^{13}), 125.09 (C^4), 119.32 (C^9), 119.17 (C^7), 59.32 (C^{17}), 44.44 (C^{11}), 39.77 (C^{16}), 17.85 (C^{15}). ESI-HRMS: exact m/z calculated for [$C_{29}H_{30}N_6ORuS$]$^{2+}$: 306.0621 m/z, found: 306.0617 m/z. Elemental analysis (%) for compound [**4b**](PF$_6$)$_2$ ($C_{29}H_{30}F_{12}N_7OP_2RuS$), calculated C, 38.63; H, 3.35; N, 9.32; found C, 38.53; H, 3.34; N, 9.30. UV-Vis (1/5 H_2O/acetone): λ_{max} (ε): 459 nm (7.3 × 10^3 $M^{-1}cm^{-1}$).

3.5.3 Single crystal X-ray crystallography

Detailed crystallographic data are provided in appendix III.1.

3.5.4 Photochemistry

Molar absorption coefficient determination

Molar absorption coefficients were determined as described in appendix I.2.1. Results for the compounds reported in this chapter are provided in appendix III.2.1.

Photosubstitution quantum yield measurements

Photon fluxes of all LEDs were determined using ferrioxalate actinometry and is described in detail in appendix I.2.2. The photosubstitution quantum yields were determined as described in appendix I.2.3.

Photosubstitution followed by ^{1}H-NMR

The ^{1}H-NMR photosubstitution experiments were performed as described in appendix I.2.6. Results for the compounds reported in this chapter are provided in appendix III.2.3.

3.6 References

(1) Papish, E. T.; Oladipupo, O. E. *Current Opinion in Chemical Biology* **2022**, *68*, 102143.

(2) Campagna, S.; Puntoriero, F.; Nastasi, F.; Bergamini, G.; Balzani, V. Photochemistry and Photophysics of Coordination Compounds: Ruthenium. In *Photochemistry and Photophysics of Coordination Compounds I*; Balzani, V., Campagna, S., Eds.; Topics in Current Chemistry; Springer Berlin Heidelberg: Berlin, Heidelberg, 2007; Vol. 280, 117–214.

(3) White, J. K.; Schmehl, R. H.; Turro, C. *Inorganica Chimica Acta* **2017**, *454*, 7–20.

(4) Bonnet, S. *J. Am. Chem. Soc.* **2023**, *145* (43), 23397–23415.

(5) L. N. Lameijer, D. Ernst, S. L. Hopkins, M. S. Meijer, S. H. C. Askes, S. E. Le Dévédec, S. Bonnet, *Angew. Chem. Int. Ed.* **2017**, *56*, 11549–11553.

(6) D. Havrylyuk, A. C. Hachey, A. Fenton, D. K. Heidary, E. C. Glazer, *Nat. Commun.* **2022**, *13*, 3636.

(7) Respondek, T.; Sharma, R.; Herroon, M. K.; Garner, R. N.; Knoll, J. D.; Cueny, E.; Turro, C.; Podgorski, I.; Kodanko, J. J. *ChemMedChem* **2014**, *9* (6), 1306–1315.

(8) Filevich, O.; Etchenique, R. *Photochem Photobiol Sci* **2013**, *12* (9), 1565–1570.

(9) Van Rixel, V. H. S.; Ramu, V.; Auyeung, A. B.; Beztsinna, N.; Leger, D. Y.; Lameijer, L. N.; Hilt, S. T.; Le Dévédec, S. E.; Yildiz, T.; Betancourt, T.; Gildner, M. B.; Hudnall, T. W.; Sol, V.; Liagre, B.; Kornienko, A.; Bonnet, S. *J. Am. Chem. Soc.* **2019**, *141* (46), 18444–18454.

(10) Hakkennes, M. L. A.; Meijer, M. S.; Menzel, J. P.; Goetz, A.-C.; Van Duijn, R.; Siegler, M. A.; Buda, F.; Bonnet, S. *J. Am. Chem. Soc.* **2023**, *145* (24), 13420–13434.

(11) Collin, J.-P.; Jouvenot, D.; Koizumi, M.; Sauvage, J.-P. *Inorganica Chimica Acta* **2007**, *360* (3), 923–930.

(12) Garner, R. N.; Joyce, L. E.; Turro, C. *Inorg. Chem.* **2011**, *50* (10), 4384–4391.

(13) Meijer, M. S.; Bonnet, S. *Inorg. Chem.* **2019**, *58* (17), 11689–11698.

(14) Pinnick, D. V.; Durham, B. *Inorg. Chem.* **1984**, *23* (10), 1440–1445.

(15) Liu, Y.; Turner, D. B.; Singh, T. N.; Angeles-Boza, A. M.; Chouai, A.; Dunbar, K. R.; Turro, C. *J. Am. Chem. Soc.* **2009**, *131* (1), 26–27.

(16) Zayat, L.; Calero, C.; Alborés, P.; Baraldo, L.; Etchenique, R. *J. Am. Chem. Soc.* **2003**, *125* (4), 882–883.

(17) Awada, A.; Loiseau, F.; Jouvenot, D. *Eur J Inorg Chem* **2021**, *2021* (44), 4539–4542.

(18) Ballester, F. J.; Hernández-García, A.; Santana, M. D.; Bautista, D.; Ashoo, P.; Ortega-Forte, E.; Barone, G.; Ruiz, J. *Inorg. Chem.* **2024**, *63* (14), 6202–6216.

(19) Coe, B. J.; Glenwright, S. J. *Coordination Chemistry Reviews* **2000**, *203* (1), 5–80.

(20) Wilson, J. J.; Lippard, S. J. *Chem. Rev.* **2014**, *114* (8), 4470–4495.

(21) Quiroga, A. G. *Journal of Inorganic Biochemistry* **2012**, *114*, 106–112.
(22) Aris, S. M.; Farrell, N. P. *Eur J Inorg Chem* **2009**, *2009* (10), 1293–1302.
(23) Rafic, E.; Slep, L. D.; Etchenique, R. *Pure and Applied Chemistry* **2023**, *95* (8), 879–889.
(24) Rojas Pérez, Y.; Slep, L. D.; Etchenique, R. *Inorg. Chem.* **2019**, *58* (17), 11606–11613.
(25) Van Rixel, V. H. S.; Moolenaar, G. F.; Siegler, M. A.; Messori, L.; Bonnet, S. *Dalton Trans.* **2018**, *47* (2), 507–516.
(26) Den Boer, D.; Konovalov, A. I.; Siegler, M. A.; Hetterscheid, D. G. H. *Inorg. Chem.* **2023**, *62* (14), 5303–5314.
(27) Havrylyuk, D.; Stevens, K.; Parkin, S.; Glazer, E. C. *Inorg. Chem.* **2020**, *59* (2), 1006–1013.
(28) Van Rixel, V. H. S.; Ramu, V.; Auyeung, A. B.; Beztsinna, N.; Leger, D. Y.; Lameijer, L. N.; Hilt, S. T.; Le Dévédec, S. E.; Yildiz, T.; Betancourt, T.; Gildner, M. B.; Hudnall, T. W.; Sol, V.; Liagre, B.; Kornienko, A.; Bonnet, S. *J. Am. Chem. Soc.* **2019**, *141* (46), 18444–18454.
(29) Meijer, M. S.; Bonnet, S. *Inorg. Chem.* **2019**, *58* (17), 11689–11698.
(30) Bahreman, A.; Limburg, B.; Siegler, M. A.; Bouwman, E.; Bonnet, S. *Inorg. Chem.* **2013**, *52* (16), 9456–9469.
(31) Johnson, B. A.; Agarwala, H.; White, T. A.; Mijangos, E.; Maji, S.; Ott, S. *Chemistry A European J* **2016**, *22* (42), 14870–14880.
(32) Knoll, J. D.; Albani, B. A.; Durr, C. B.; Turro, C. *J. Phys. Chem. A* **2014**, *118* (45), 10603–10610.
(33) Yang, L.; Powell, D. R.; Houser, R. P. *Dalton Trans.* **2007**, *9*, 955–964.
(34) Marchivie, M.; Guionneau, P.; Létard, J.-F.; Chasseau, D. *Acta Crystallogr B Struct Sci* **2005**, *61* (1), 25–28.
(35) Rafic, E.; Slep, L. D.; Etchenique, R. *Pure and Applied Chemistry* **2023**, *95* (8), 879–889.
(36) Havrylyuk, D.; Deshpande, M.; Parkin, S.; Glazer, E. C. *Chem. Commun.,* **2018**, *54*, 12487–12490.
(37) Cuello-Garibo, J.-A.; Meijer, M. S.; Bonnet, S. *Chem. Commun.* **2017**, *53* (50), 6768–6771.
(38) Steinke, S. J.; Piechota, E. J.; Loftus, L. M.; Turro, C. *J. Am. Chem. Soc.* **2022**, *144* (44), 20177–20182.
(39) Malouf, G.; Ford, P. C. *J. Am. Chem. Soc.* **1977**, *99* (22), 7213–7221.
(40) Shaw, L. E.; Langford, C. H. *Inorg. Chem.* **2000**, *39* (3), 541–546.
(41) Vichova, J.; Hartl, F.; Vlcek, A. *J. Am. Chem. Soc.* **1992**, *114* (27), 10903–10910.
(42) Pižl, M.; Hunter, B. M.; Sazanovich, I. V.; Towrie, M.; Gray, H. B.; Záliš, S.; Vlček, A. *Inorg. Chem.* **2022**, *61* (6), 2745–2759.
(43) Verbeet, W.; Husiev, Y.; Bonnet, S. *Eur J Org Chem* **2024**, *27* (14), e202400054.
(44) Zhou, X.-Q.; Xiao, M.; Ramu, V.; Hilgendorf, J.; Li, X.; Papadopoulou, P.; Siegler, M. A.; Kros, A.; Sun, W.; Bonnet, S. *J. Am. Chem. Soc.* **2020**, *142* (23), 10383–10399.